

1

2 **Assessment of landscape-scale fluxes of carbon dioxide and methane in subtropical**
3 **coastal wetlands of South Florida**

4 **Erin R. Delaria^{1,2,3}, Glenn M. Wolfe¹, Kaitlyn Blanock⁴, Reem Hannun^{4†}, Kenneth Lee**
5 **Thornhill^{5,6}, Paul A. Newman¹, Leslie R. Lait^{1,7}, S. Randy Kawa¹, Jessica Alvarez⁸, Spencer**
6 **Blum⁸, Edward Castañeda-Moya⁹, Christopher Holmes⁸, David Lagomasino¹⁰, Sparkle**
7 **Malone¹¹, Dylan Murphy⁸, Steven F. Overbauer⁹, Chandler Pruett⁸, Aaron Serre⁸, Gregory**
8 **Starr¹², Robert Szot⁸, Tiffany Troxler¹³, David Yannick¹², Benjamin Poulter¹⁴**

9 ¹Atmospheric Chemistry and Dynamics Laboratory, NASA Goddard Spaceflight Center,
10 Greenbelt, MD, 20771, USA. ²NASA Postdoctoral Program, Oakridge Associated Universities,
11 Oak Ridge, TN, 37831. ³Earth System Science Interdisciplinary Center, University of Maryland,
12 College Park, MD 20740. ⁴Department of Geology and Environmental Science, University of
13 Pittsburg, Pittsburgh, PA, 15260, USA. ⁵NASA Langley Research Center, Hampton, VA, 23666,
14 USA. ⁶Analytical Mechanics Associates (AMA), Hampton, VA 23666. ⁷Science Systems and
15 Applications, Inc., Lanham, MD, USA. ⁸The Department of Earth, Ocean, and Atmospheric
16 Science, Florida State University, Tallahassee, FL, 32304, USA. ⁹Department of Biological
17 Sciences, Florida International University, Miami, FL, 33199, USA. ¹⁰Department of Coastal
18 Studies, East Carolina University, Greenville, NC, 27858, USA. ¹¹Yale School of the
19 Environment, Yale University, New Haven, CT, 06511, USA. ¹²Department of Biological
20 Sciences, University of Alabama, Tuscaloosa, AL 35487, USA. ¹³ Department of Earth and
21 Environment, Florida International University, Miami, FL, 33199, USA. ¹⁴ Biospheric Sciences
22 Laboratory, NASA Goddard Space Flight Center, Greenbelt, MD 20771, USA.

23

24 Corresponding author: Erin R. Delaria (erin.r.delaria@nasa.gov)

25 † Current address: Atmospheric Science Branch, NASA Ames Research Center, Moffett Field,
26 CA, 94035, USA

27 **Key Points:**

- 28
- Airborne eddy covariance measurements reveal heterogeneity in CH₄ and CO₂ fluxes
29 across southern Florida.
 - Variability in carbon fluxes were primarily driven by vegetation types, season, ecosystem
30 productivity, and soil inundation.
 - Southern Florida served as a net carbon sink during all flight periods, with CH₄ emissions
31 offsetting CO₂ deposition by 11-91%.
- 32
- 33
- 34
- 35
- 36

37 **Abstract**

38 Coastal wetlands play a significant role in the storage of 'blue carbon', indicating their
39 importance in the carbon biogeochemistry in the coastal zone and in global climate change
40 mitigation strategies. We present airborne eddy-covariance observations of CO₂ and CH₄ fluxes
41 collected in southern Florida as part of the NASA BlueFlux mission during April 2022, October
42 2022, February 2023, and April 2023. The flux data generated from this mission consists of over
43 100 flight hours and more than 6000 km of horizontal distance over coastal saline and freshwater
44 wetlands. We find that the spatial and temporal heterogeneity in CO₂ and CH₄ exchange is
45 primarily influenced by season, vegetation type, ecosystem productivity, and soil inundation.
46 The largest CO₂ uptake fluxes of more than -20 μmol m⁻² s⁻¹ were observed over mangroves
47 during all deployments and over swamp forests during flights in April. The greatest CH₄ effluxes
48 of more than 250 nmol m⁻² s⁻¹ were measured at the end of the wet season in October 2022 over
49 freshwater marshes and swamp shrublands. Although the combined Everglades National Park
50 and Big Cypress National Preserve region was a net sink for carbon, CH₄ emissions reduced the
51 ecosystem carbon uptake capacity (net CO₂ exchange rates) by 11-91%. Average total net carbon
52 exchange rates during the flight periods were -4 to -0.2 g CO₂-eq m⁻² d⁻¹. Our results highlight
53 the importance of preserving mangrove forests and point to potential avenues of further research
54 for greenhouse gas mitigation strategies.

55 **Plain Language Summary**

56 Coastal wetlands play a crucial role in trapping and storing carbon, aiding in climate change
57 adaptation and mitigation efforts. Carbon dioxide (CO₂) uptake and methane (CH₄) emissions
58 were measured from an aircraft over wetlands of southern Florida during different times of the
59 year. Season, vegetation, and water depth were found to have a large influence on carbon
60 exchange. Mangroves with the largest canopy heights showed the highest CO₂ uptake, while CH₄
61 emissions peaked during the wet season over freshwater marshes where surface water depths
62 were greatest. CH₄ emissions diminished the overall carbon uptake capacity of southern Florida.
63 Results emphasize the importance of preserving coastal wetland ecosystems and suggest
64 potential directions for further research aimed at mitigating greenhouse gas emissions.

65 **1 Introduction**

66 Vegetated ecosystems mitigate the impact of anthropogenic CO₂ emissions by serving as
67 natural carbon stores (e.g., Barbier et al., 2011; Donato et al., 2011; Murdiyarso et al., 2015;
68 Duarte 2017). The terrestrial biosphere is estimated to remove 10—40 % of the CO₂ emitted
69 from fossil fuels, and coastal aquatic vegetation removes a further 3—25% (Barbier et al., 2011;
70 Donato et al., 2011; Murdiyarso et al., 2015; Duarte 2017; Friedlingstein et al., 2023). Coastal
71 vegetated ecosystems have been of recent interest for “blue” carbon mitigation strategies because
72 of their efficiency for short-term carbon storage in vegetation biomass (above- and belowground)
73 and long-term carbon storage in soils and sediments (e.g., McLeod et al., 2011; Barbier et al.,
74 2011; Donato et al., 2011; Murdiyarso et al., 2015; Macreadie et al., 2021; Poulter et al., 2023).
75 “Blue” carbon refers to the carbon that is captured by oceans and coastal ecosystems. Although
76 coastal vegetated ecosystems (i.e., mangroves, salt marshes, seagrasses) cover an area equivalent
77 to ~2% of terrestrial forest area, their carbon burial rates are 50 times faster per unit area,
78 making the net contributions of coastal wetlands to carbon sequestration comparable to that of
79 terrestrial forests (McLeod et al., 2011; Duarte et al., 2013). Yet these ecosystems are under

80 continued threat due to hurricanes, land development, and sea level rise, which contribute to a
81 global net loss of mangroves and salt marshes at a rate of 0.13—2 % annually (McLeod et al.,
82 2011; Goldberg et al., 2020; Campbell et al., 2022; Murray et al., 2022).

83 Understanding the climate change mitigation potential of these ecosystems requires
84 accurate accounting of their carbon balance. Only a fraction of the CO₂ taken up by coastal
85 vegetation is sequestered in sediments via long-term carbon burial. Much of this carbon is stored
86 in shorter-term above- and belowground biomass, re-emitted to the atmosphere through soil
87 respiration, or transported to the ocean as particulate organic carbon (POC), dissolved organic
88 carbon (DOC), and dissolved inorganic carbon (DIC) (Rosentreter 2018b; Sanderman et al.,
89 2018; Simard et al., 2019; Adame et al., 2021). In addition, anoxic soil conditions and
90 methanogenic archaea in coastal vegetated ecosystems produce CH₄ (e.g. Bartlett et al., 1987;
91 Rosentreter 2018c; Al-Haj and Fulweiler, 2020). Methane emissions have the potential to
92 significantly offset the climate mitigation potential of coastal wetlands, as the global warming
93 potential (GWP) of methane is 81.2 and 27.9 times greater than that of CO₂ on a 20- and 100-
94 year scale, respectively (Forster et al., 2021). Estimates of global CH₄ emissions from coastal
95 wetlands are poorly constrained, with uncertainties stemming from large regional differences,
96 lack of direct measurements, and anthropogenic impacts on wetland disturbance and hydrology
97 (Harrison et al., 2017; Kroeger et al., 2017; Saunio et al., 2020; Rosentreter et al., 2021).

98 Several methods exist for quantifying carbon exchange at landscape to global scales, each
99 with their own benefits and limitations. Concentration measurements from aircraft, ground sites,
100 and satellites can be coupled with inverse models to provide a “top-down” inference of
101 atmosphere-biosphere CO₂ and CH₄ exchange (e.g. Wang et al., 2018; Saunio et al., 2020; Ma
102 et al., 2021; Schiferl et al., 2022; Gaubert et al., 2023). However, these top-down approaches
103 suffer from considerable uncertainties related to atmospheric transport and heavily rely on prior
104 assumptions for source attribution. Satellite-based top-down approaches allow for the assessment
105 of changes in CO₂ and CH₄ fluxes over multiple years with global coverage, which is particularly
106 important in areas where direct ground-based and airborne measurements are limited (e.g.,
107 Campbell et al., 2020). Satellite approaches are, however, further limited by additional
108 uncertainties related to satellite retrievals. Bottom-up inferences of carbon atmosphere-biosphere
109 exchange in wetlands utilize biophysical process models, inventories of biomass, and remotely
110 sensed surface properties to indirectly calculate fluxes (Hayes et al., 2018; Saunio et al., 2020;
111 Ma et al., 2021; Friedlingstein et al., 2022; Zhang et al., 2023). These models, however, rely on
112 complicated parameterizations and assumptions of biological activity across a complex diversity
113 of ecosystems and environmental conditions. This leads to large uncertainties, disagreements
114 between different modeling approaches, and inconsistencies between top-down and bottom-up
115 approaches (Melton et al., 2013; Pandey et al., 2021; Saunio et al., 2020; Ma et al., 2021).

116 Alternatively, atmosphere-biosphere fluxes can also be measured directly on a variety of
117 scales and can provide a more discerning understanding of wetland fluxes in space and time.
118 Ground-based chamber measurements are important for quantifying process-level drivers of
119 carbon exchange from soils, leaves, roots, and stems (e.g. Nahlik and Mitsch 2011; Marín-Muñiz
120 et al., 2015; Troxler et al., 2015; Rosentreter et al., 2018a). Chamber water-atmosphere CH₄ and
121 CO₂ fluxes coupled to measurements of water properties have identified factors controlling the
122 cycling of carbon in mangrove-dominated Australian estuaries and tidal freshwater marshes in
123 Veracruz, Mexico (Marín-Muñiz et al., 2015; Rosentreter et al., 2018a). These types of studies
124 are extremely useful for linking carbon fluxes to underlying processes, but measurements are

125 typically only conducted for a short period of time at a limited number of sites, making upscaling
126 these findings difficult and sensitive to statistical assumptions.

127 Eddy covariance flux towers provide localized representations of net ecosystem exchange
128 (NEE) fluxes over longer periods (e.g., Barr et al., 2010; Beringer et al., 2013; Malone et al.,
129 2015; Shoemaker et al., 2015; Alvarado-Barrientos 2020; Zhu et al., 2021). Such EC towers have
130 been used to quantify the seasonality of net ecosystem CO₂ exchange in mangrove forests in the
131 Florida Everglades (Barr et al., 2010; Barr et al., 2012), the Yucatan Peninsula (Alvarado-
132 Barrientos 2020), and southeastern China (Zhu et al., 2021). But the degree to which
133 measurements at one flux tower are representative of other sites varies, even within the same
134 region, as environmental conditions (e.g. soil properties, inundation, leaf area, tidal influence,
135 etc.) can vary from region to region and from site to site.

136 Airborne eddy covariance (EC) offers a viable approach to measure fluxes over larger
137 areas, though with a more limited temporal resolution (e.g. Crawford et al., 1996; Sellers et al.,
138 1997; Zulueta et al., 2013; Wolfe et al., 2015; Desjardins et al., 1982; Wolfe et al., 2018; Hannun
139 et al., 2020). This technique has the advantage of elucidating heterogeneous fluxes over a large
140 region (15-100 km) at a relatively fine spatial scale (~1km). One recent application of the
141 technique in a tropical Zambian wetland highlighted large discrepancies between land surface
142 models and observations (Shaw et al., 2022). Zulueta et al. (2013) also utilized airborne EC to
143 derive heterogeneous CO₂ fluxes over distinct ocean, mangrove, and desert ecosystems in Baja
144 California Sur, Mexico. This latter study also utilized tower flux measurements and vegetation
145 indices to assess the representativeness of towers and provide a simple model for scaling up to
146 regional CO₂ fluxes. However, these studies represent two of only very few that have used
147 airborne EC to measure greenhouse gas exchange in subtropical to tropical wetlands.

148 Here we analyze extensive airborne CO₂ and CH₄ flux measurements acquired over
149 southern Florida during the NASA BlueFlux mission. Combining flux measurements and flux
150 footprint analysis with detailed information of land surface properties, we explore the patterns in
151 flux variability across this diverse landscape. We also utilize long-term ground-based flux
152 datasets to provide a valuable point of comparison and a means of upscaling to estimate the net
153 regional carbon balance. Although the definition of “blue” carbon typically only includes tidal
154 saltwater wetlands, we also investigate carbon exchange in the freshwater wetlands within the
155 greater Everglades coastal watershed system. These regions are also extremely influential in the
156 carbon cycle of this coastal zone. The primary objectives of this study are to 1) elucidate the
157 heterogeneity of atmosphere-biosphere carbon fluxes in southern Florida, 2) identify the
158 underlying sources of this variability, and 3) provide an estimate of the net carbon balance during
159 the sampling periods from an atmospheric perspective. In addressing each of these objectives, we
160 identify potential avenues for applying our unique data set to addressing “blue” carbon
161 greenhouse mitigation strategies.

162

163 **2 Materials and Methods**

164 **2.1 BlueFlux Field Campaign**

165 BlueFlux is a NASA-sponsored effort to understand the dynamics of carbon exchange in
166 coastal wetlands and develop long-term gridded flux estimates for science and policy

167 applications. The BlueFlux field campaign was developed to provide comprehensive
168 measurements of ecosystem carbon fluxes in southern Florida, with a special emphasis on
169 mangroves. BlueFlux observations bridge multiple scales of biosphere-atmosphere exchange,
170 including chamber measurements of soil and vegetation fluxes, ecosystem-scale fluxes from
171 existing EC tower sites, airborne EC measurements across the south Florida region, and lateral
172 aquatic carbon fluxes (Poulter et al., 2023). Primary study regions include Everglades National
173 Park (ENP) and Big Cypress National Preserve (BCNP) (Fig. 1). The focus of this study is the
174 airborne EC component of the project.

175 Southern Florida is characterized by a subtropical to tropical climate. The wet season
176 occurs from May—October, during which conditions are hot ($>30^{\circ}\text{C}$) and humid ($>80\%$ relative
177 humidity) with frequent convective thunderstorms. The average annual rainfall is typically
178 1000—1700 mm, with 70% of precipitation occurring during the wet season (Florida Climate
179 Center <https://climatecenter.fsu.edu/products-services/data/statewide-averages/precipitation>).
180 The dry season (November to April) is typically warm ($13\text{—}22^{\circ}\text{C}$) and dryer, with very rare
181 winter frosts projected to decrease over time (Ross et al., 2009). Flights were performed during
182 April 2022, October 2022, February 2023, and April 2023. April months are typically in the tail-
183 end of the dry season and beginning of the wet season, while October is considered the tail-end
184 of the wet season. Temperatures during study months were roughly average for the area and
185 season, and ENP and BCNP experienced an average amount of rainfall during April 2022 and
186 October 2022. However, Hurricane Ian made landfall north of the study region on September 28,
187 2022. There were higher observed water levels in the weeks following the hurricane at EC tower
188 sites (EDEN, <https://sofia.usgs.gov/eden>). Conversely, February 2023 and April 2023 experienced
189 below average rainfall by 26% and 73%, respectively (South Florida Water Management District
190 <https://www.sfwmd.gov/weather-radar/rainfall-historical/year-to-date>). Atlantic basin hurricanes
191 frequently pass over Southern Florida between August and November. Such hurricanes have
192 resulted in significant alteration to the coastal wetlands of Southern Florida over the past 32
193 years (Taillie et al., 2020). The terrain is mostly flat, with some small hills (up to 6 m above
194 mean sea level) in the northwest portion of BCNP.

195

196 2.2 Airborne flux measurements

197 2.2.1 Flight strategy

198 Airborne operations utilized a Beechcraft King Air A90 owned and operated by Dynamic
199 Aviation. Deployments entailed four 2-week intensives, each consisting of 6 – 8 flights with
200 durations of 2 – 4 hours each (~ 25 flight hours per deployment). A typical flight consisted of
201 straight and level legs at an altitude of 90 m above mean sea level and a ground speed of 65 – 80
202 m s^{-1} , along with occasional overlapping legs at higher altitudes (up to 300 m) to constrain flux
203 divergence. Vertical profiles were performed periodically (up to 3 km) to ascertain boundary
204 layer depth. Flux legs were typically oriented across the mean horizontal wind flow, spanned
205 lengths of 20 – 100 km, and concentrated on mangrove forests and regions of recent mangrove
206 dieback ('ghost' forests) (Fig. 1) that resulted from impacts of Hurricane Irma (September 2017)
207 (Lagomasino et al., 2021). Other considerations for flight design included overflight of existing
208 ground sites and avoidance of nesting bird colonies and Seminole and Miccosukee tribal lands.

209 In total, flux transects during all deployment periods comprise more than 6000 km of linear
 210 distance.

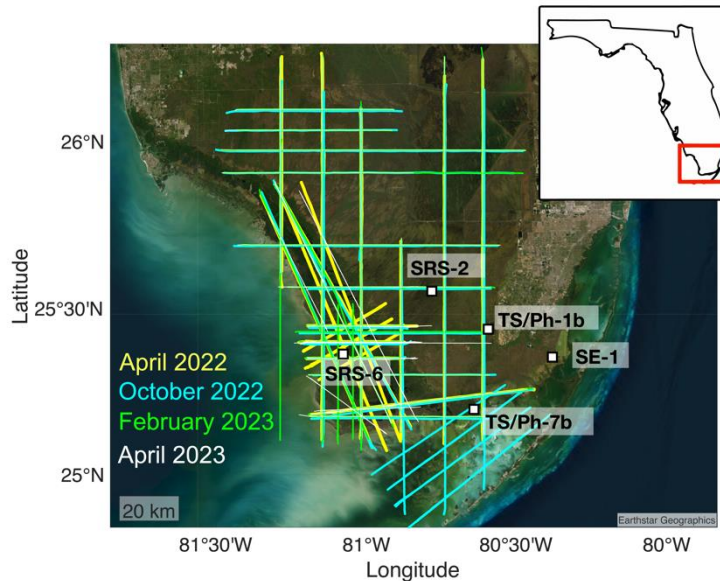


Figure 1: Flux transects from all flights between April 2022 and April 2023. Flux legs from April 2022, October 2022, February 2023, and April 2023 are shown in yellow, cyan, green, and white, respectively. The locations of five ground sites with eddy covariance towers are indicated with square markers.

211

212 2.2.2 Instrument Payload

213 The BlueFlux study utilized an upgraded version of the NASA Carbon Airborne Flux
 214 Experiment (CARAFE) platform, originally described by Wolfe et al (2018). Ambient air was
 215 sampled from a common inlet (1.3 cm stainless steel with fluoropel coating) located under right
 216 wing. The sample tube was fluorinated ethylene propylene (FEP) with an inner diameter of 0.65
 217 cm and a length of about 8 m. Gas measurements utilized two commercial Picarro closed-path
 218 analyzers. A model g2311f (hereafter, PFlux) provided continuous measurements of CH₄, CO₂
 219 and H₂O at 10 Hz, while a model g2401m (hereafter PConc) provided measurements of CH₄,
 220 CO₂, H₂O, and CO at 0.5 Hz. Agilent IDP3 scroll pumps maintained gas flows of ~5.5 slm and
 221 ~1 slm, respectively. The greater pressure stability of the PConc (which is designed for flight)
 222 provides an accuracy standard, while the PFlux provided the fast measurements required for
 223 eddy covariance. Supplement Section S1 describes comparisons and corrections for the two
 224 instruments. The PConc was calibrated in the lab before and after each mission (see Sect 2.2.3).

225 An Aventech Aircraft-Integrated Meteorological Measurement System (AIMMS-20)
 226 provided 20 Hz measurements of aircraft position and attitude, air temperature and pressure, and
 227 3-D wind velocities. The probe was mounted under the left wing and calibrated via the
 228 manufacturer-provided protocol at the start of each deployment.

229 2.2.3 Flux calculations

230 Data from the AIMMS-20 probe (20-Hz vertical wind speed, w , and potential
231 temperature, θ), and the 10 Hz measurement of H_2O , CO_2 , and CH_4 were time aligned to a
232 common 10-Hz time base and combined to determine fluxes of CH_4 , CO_2 , latent heat (LE) and
233 sensible heat (H) using airborne eddy covariance with the continuous wavelet transform (CWT)
234 method (Torrence and Compo, 1998; Wolfe et al., 2018). Flux legs were selected as flight
235 segments greater than 15 km in linear distance with an aircraft roll not exceeding 5° and altitude
236 variation within ± 10 m. Scalar time series were detrended by subtracting a 40-second (~ 4 km)
237 moving average and time-shifted by 0 to 3 s based on lag correlation to the vertical wind (Fig.
238 S4). This detrending length was selected to remove non-turbulent variability and maintain the
239 largest eddies contributing to the flux (Moncrieff et al., 2006).

240 Following this pre-processing of the data, fluxes were calculated using CWT (Section
241 S2). Flux data for analysis is filtered by the cone of influence (COI), i.e., the spectral region
242 where additional errors and uncertainties may be present due to edge effects (Torrence and
243 Compo, 1998). Data are excluded where the fraction of the cospectral power that resides within
244 the COI is greater than 0.5. Fluxes are further filtered to exclude measurements where the
245 friction velocity (u^*)—as determined from momentum fluxes at aircraft height (Section 2.4.3)—
246 is less than 0.2 m s^{-1} over land, or less than 0.1 m s^{-1} over water. This criterion was selected to
247 exclude periods with insufficient vertical mixing (e.g. Hogstrom 1988; Barr et al., 2010; Hayek
248 et al., 2018). The selected u^* filtering limits are in accordance with EC towers (Barr et al., 2010)
249 and were verified for flight data with the method of Hayek et al., 2018.

250 2.2.4 Uncertainties

251 Systematic error contributions to flux uncertainties include those due to under-sampling
252 of low frequencies (SE_{turb}), the instrument response time which can limit detection of high-
253 frequency signals (SE_{RT}), and instrument accuracy (SE_{acc}). SE_{RT} and SE_{turb} were calculated
254 according to Wolfe et al., 2018. The e-folding response time used to calculate SE_{RT} was
255 determined through laboratory tests to be 90 ± 10 ms for the PFlux instrument—which translates
256 to an effective cutoff frequency of 3.8 Hz. SE_{acc} for each scalar is based on measurement
257 accuracy. Accuracy for CH_4 and CO_2 measurements are 0.05%, and 0.2%, respectively,
258 determined through laboratory calibration with WMO-grade calibration NOAA cylinders (IDs
259 CC746186 and CA03516). The PFlux stated H_2O accuracy is 0.8%. The AIMMS-20 probe has a
260 stated accuracy of 10% for vertical wind speed.

261 Random errors in fluxes include contributions from uncorrelated instrument noise and
262 turbulent variability. Methods have been developed for traditional ensemble-averaged EC to
263 represent the individual contributions of these two sources of uncertainty, as well as to
264 empirically calculate the total random error based on the cross- and auto- covariance of scalar s
265 and w at different time lags (e.g. Leschow et al., 1994, Finkelstein and Simms, 2001). It is not
266 immediately obvious how these approaches are best applied to time-resolved CWT analysis.
267 Here we propose a new method for quantifying random flux errors (RE) for CWT based upon
268 Langford et al. (2015). In this approach, the root mean squared deviation from zero of the cross-
269 covariance between s and w is used to represent the random flux error (RE):

$$RE = \sqrt{N} \sqrt{\left(0.5 \left((\sigma_{w's'[-\Gamma]})^2 + (\overline{f_{w's'[-\Gamma]}})^2 + (\sigma_{f_{w's'[\Gamma]}})^2 + (\overline{f_{w's'[\Gamma]}})^2 \right)\right)^2} \quad (1)$$

271 Here N is the number of data points per second, $\sigma_{w's'}$ is the standard deviation of the covariance
 272 ($f_{w's'}$) and $\overline{f_{w's'}}$ is the average cross-covariance over a time lag range of $-\Gamma$ or $+\Gamma$. Primes
 273 denote deviations from the mean of w and s . We define Γ over a time lag range from one to 100
 274 data points. Here, 100 was chosen as the maximum lag considered for Γ to be representative of
 275 the integral time scale. This representation considers the variability in the cross-covariance of s
 276 and w , as well as the offset from zero related to non-turbulent trends in the data.

277 Random flux errors vary along flux legs due to variations in turbulence and tend to be
 278 larger in magnitude for larger magnitude fluxes. For 1 Hz-averaged flux measurements, the

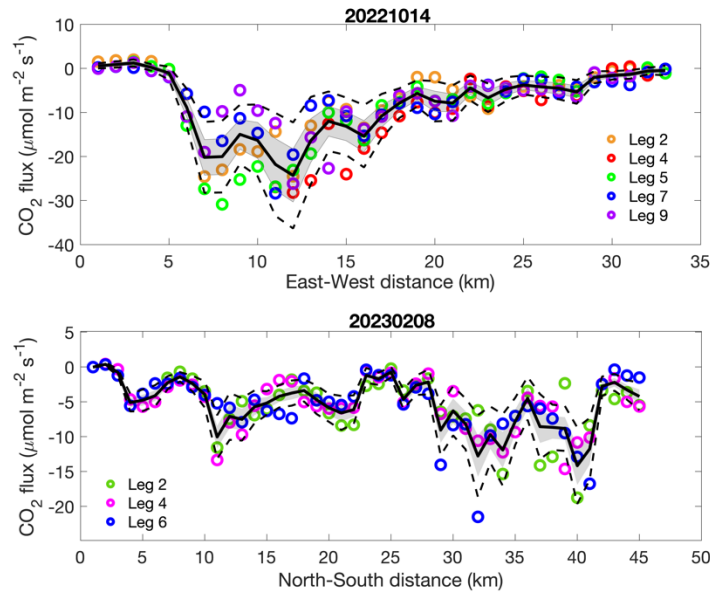


Figure 2: CO₂ fluxes for repeated legs over the same flight path on October, 14, 2022 (top) and February 8, 2023 (bottom). Colored markers represent 1 km average fluxes for the different legs. Solid black lines, shading, and dotted lines represent the mean flux, 1 σ random error, and 2 σ random error, respectively.

279 median limit of detection (LOD), defined as twice the median random flux error, is 2.8 $\mu\text{mol m}^{-2}$
 280 s^{-1} and 18.3 $\text{nmol m}^{-2} \text{s}^{-1}$ for CO₂ and CH₄ fluxes, respectively. Average fluxes at 1 km resolution
 281 have a median LOD of 0.9 $\mu\text{mol m}^{-2} \text{s}^{-1}$ and 5.8 $\text{nmol m}^{-2} \text{s}^{-1}$ for CO₂ and CH₄ fluxes,
 282 respectively. This error is approximately a factor of three lower than that derived using the
 283 approach of Wolfe et al. (2018), which was calculated from the sum (rather than the standard
 284 deviation and mean) of the cross covariance between s and w in analogy to Finkelstein and Sims
 285 (2001). Random fluxes were also estimated experimentally over a leg on April 19, 2022, by
 286 overflowing the inlet with calibration gas. The standard deviation of the 10 Hz CO₂ “flux” was
 287 0.7 $\mu\text{mol m}^{-2} \text{s}^{-1}$ (mean -0.0045 $\mu\text{mol m}^{-2} \text{s}^{-1}$), providing an estimation of combined instrument
 288 noise and turbulence random errors over this leg. We found the approach of Wolfe et al. (2018)

289 to result in an unreasonably large random flux error over the same flight track of $9.0 \mu\text{mol m}^{-2} \text{s}^{-1}$,
290 1 , compared with our new parameterization ($3.3 \mu\text{mol m}^{-2} \text{s}^{-1}$) (Figure S11).

291 During each flight we performed repeat flux legs over the same ground track above a
292 mangrove forest to provide an additional test of the variability in flux measurements due to
293 random error. Figure 2 shows 1 km averaged CO_2 fluxes from repeat legs during two different
294 flight patterns flown in October 2022 and February 2023. Leg-to-leg variability typically falls
295 within that expected based on random errors estimated via Eqn. (1), providing further validation
296 of the calculated random flux errors.

297 We include an additional uncertainty estimate from the vertical divergence of fluxes (see
298 Supplementary Information Section S5). During each flight we performed vertically stacked legs
299 to estimate the change in flux with altitude and allow for extrapolation of fluxes to the surface. In
300 most cases the differences in calculated surface fluxes and fluxes measured at the aircraft altitude
301 ($< 100 \text{ m}$) were not statistically significant ($\alpha = 0.05$, two-sided t-test). This is not surprising, as
302 the aircraft altitude was typically in the lowest 10 % of the boundary layer. We therefore assume
303 that the surface fluxes are equal to the aircraft altitude fluxes and include the difference between
304 the extrapolated surface flux and flux measured at the aircraft altitude as an additional systematic
305 error. We do not correct the reported fluxes for the calculated surface flux divergence because
306 this correction uncertainty is typically much larger in magnitude than the correction itself, which
307 would thus introduce even greater uncertainty. The magnitudes of all contributing flux errors are
308 shown in Figure S12. The largest sources of systematic uncertainty are divergence effects (IQR
309 3-30%) and SE_{acc} (10%). The effect of RE is small when averaged over a flux leg (IQR 1-5%
310 uncertainty), but large for 1 Hz fluxes (IQR 30 – 60 % uncertainty)

311 2.3 Flux towers

312 Several flux towers located in the Everglades regions of southern Florida measure half-
313 hourly fluxes of CO_2 , CH_4 , sensible heat (H), and latent energy (LE) using the eddy covariance
314 method. These towers are part of the Florida Coastal Everglades Long-Term Ecological
315 Research (FCE LTER) Network and the AmeriFlux tower networks. Towers are located along
316 the Shark River Slough (SRS) and the Taylor Slough/Panhandle (TS/Ph) (Fig. 1) hydrologic
317 gradients (Barr et al., 2010; Malone et al., 2015) and are representative of freshwater marsh
318 (SRS-2), freshwater marsh prairies (TS/Ph-1), mangrove forests (SRS-6) and mangrove scrub
319 (TS/Ph-7). These EC towers measure vertical wind speed and virtual temperature with 3D sonic
320 anemometers (SRS-6: model RS-50, Gill Co., Lymington, England; SRS-2, TS/Ph-7, and TS/Ph-
321 1: CSAT 3B, Campbell Scientific Inc., Logan, Utah). $\text{CO}_2/\text{H}_2\text{O}$ (LI-7500) and CH_4 (LI-7700) are
322 measured at 20 Hz with open path infrared gas analyzers (LI-COR, Inc., Lincoln, Nebraska).

323 2.4 Flux decomposition by land classification

324 Southern Florida is a heterogenous landscape with a wide range of vegetation types.
325 Vegetation phenology, quantity, and productivity modulate CO_2 uptake. Other features like
326 salinity, water levels, surface water extent, tides, inundation period, and soil moisture can lead to
327 changes in CH_4 emission fluxes and biological CO_2 respiration. We consider several
328 geographical data sets to identify some of the causes of the observed variability in GHG fluxes
329 across the flight domain.

330 2.4.1 Vegetation coverage

331 Land cover and vegetation information for ENP and BCNP was obtained from Ruiz et al.
 332 (2019, 2021) and Whelan et al. (2020). Land classifications based on these data sets included 16
 333 different classes (Fig. 3) at 50 m spatial resolution. Dominant land classifications sampled during
 334 BlueFlux over ENP and BCNP were freshwater marsh (21%), mangrove forest (17%), mangrove
 335 scrub (10%), mangrove shrubland (6.6%), salt marsh (2.2%), swamp forest (6.9%), swamp scrub
 336 (7.5%), swamp shrubland (5.7%), and upland forest (3.5%). The “Ghost Forest” land class was
 337 added to identify where mangrove forests experienced extensive die-offs by drowning following
 338 Hurricane Irma in 2017 (Lagomasino et al., 2021). Ghost forests constituted 2.2% of all land
 339 classes sampled, and 13% of the mangrove forest sampled. Dominant vegetation species found in
 340 each class are listed in Supplementary Information Section S3. Some flight tracks are outside of
 341 the ENP and BCNP boundaries and are therefore not included in the vegetation analysis.

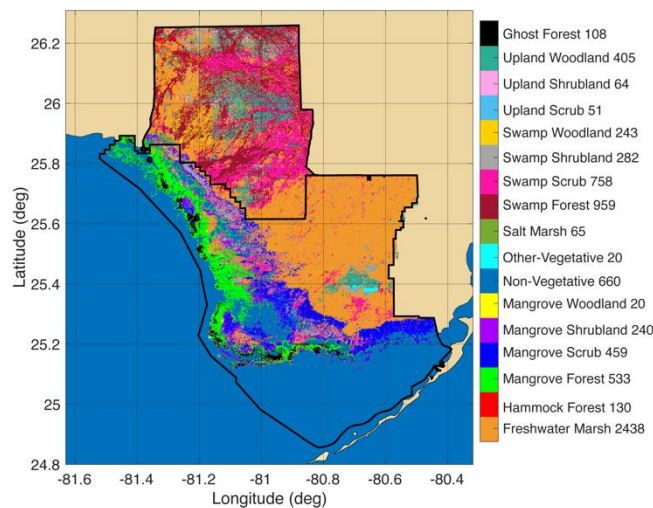


Figure 3: Map of vegetation coverage for the Everglades National Park (ENP) and Big Cypress National Preserve (BCNP) regions. Figure adapted from Ruiz et al. (2019, 2021) and Whelan et al., (2020). The ghost forest area was adapted from Lagomasino et al. (2021). Numbers following the vegetation types in the figure legend denote the area of each region in units of km². Black solid lines denote the boundaries of ENP in the south and BCNP in the north.

342 2.4.2 Other surface characteristics

343 Remotely sensed satellite products of enhanced vegetation index (EVI), normalized
 344 difference vegetation index (NDVI), leaf area index (LAI), the fraction of photosynthetically
 345 active radiation (400-700 nm) absorbed by green vegetation (FPAR), and soil moisture were
 346 obtained over South Florida as an average for each flight month. The vegetation indices were
 347 obtained from the Moderate Resolution Imaging Spectroradiometer (MODIS) on the Terra
 348 satellite at a resolution of 250 m (Didan et al., 2015). LAI and FPAR were acquired from the
 349 combined MODIS Terra + Aqua land data products at 500 m resolution (Myneni et al., 2015).

350 The Soil Moisture Active Passive mission (SMAP) provided a remotely sensed soil moisture
 351 product at 9 km resolution (O'Neil et al., 2023). Above ground biomass density (AGBM) and
 352 canopy heights for the study region were estimated from the Global Ecosystem Dynamics
 353 Investigation (GEDI) Lidar 2021 data products at 1 km resolution (Dubayah et al., 2021, 2023).

354 The Everglades Depth Estimation Network (EDEN, <https://sofia.usgs.gov/eden>) provides a
 355 long-term daily estimate of surface water-level. This data set consists of surface water depth
 356 estimates at 400 m resolution obtained from a model that interpolates measurements from a
 357 dense network of water gauges through the Everglades and water management areas of South
 358 Florida (Haider et al., 2020).

359 2.4.3 Footprint analysis

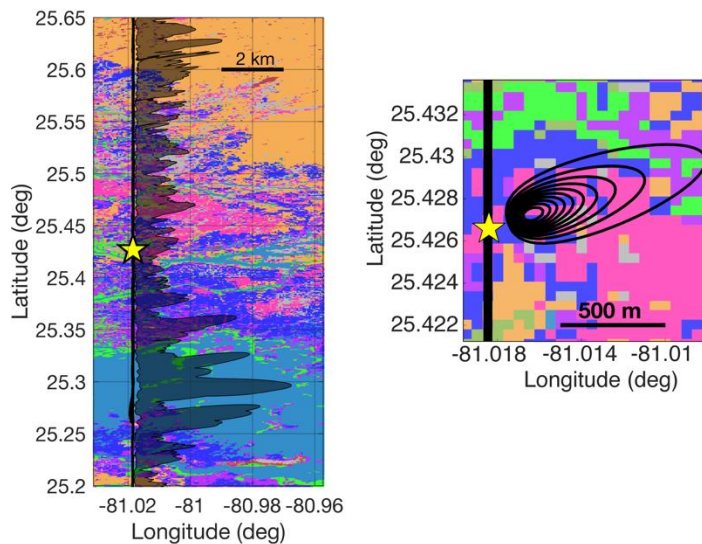


Figure 4: (Left) a single flux transect at 90 m altitude from the flight on April 19, 2023 superimposed on the map of vegetation cover. The shaded area shows the cumulative footprint containing the area contributing to 90% of the flux signal. (Right) A single footprint at the measurement location marked with the star. Contours depict the weighted contributions to the observed flux from 10% to 90% in 10% increments. Background colors denote land classification (Fig. 2).

360 Along each flux segment below 100 m altitude we computed a 2D flux footprint that
 361 expresses the relative contribution of each upwind surface element to the observed flux. This
 362 footprint analysis is detailed in Hannun et al. (2020). Briefly, to compute the flux footprint we
 363 used the parameterization of Kljun et al. (2015) based on a Lagrangian stochastic particle
 364 dispersion model (Kljun et al., 2002). Inputs to the 2D footprint calculation include the
 365 measurement height, mean horizontal wind speed (U), planetary boundary layer (PBL) height,
 366 the Obukhov length (L_{OB}), standard deviation of the lateral velocity fluctuations (σ_v), and the
 367 friction velocity (u^*). For these calculations we used the PBL height obtained from the High-
 368 Resolution Rapid Refresh (HRRR) 3 km product interpolated along our flight track. HRRR PBL
 369 height was validated against single-point determinations of actual PBL height based on

370 observations of trace gas vertical profiles during each flight. We calculated u^* from the
 371 momentum fluxes of the horizontal winds u and v (also determined with the CWT) and validated
 372 u^* with measurements from the Everglades network of EC towers (Fig. S13 and S14). The flux
 373 footprint was then rotated into the mean wind direction and translated to geographical
 374 coordinates. Example flux footprints along a flight track are shown in Figure 4. For segments
 375 below 100 m altitude, 90 % of the flux signal is contained within a region 1–2 km up wind of
 376 the measurement location over land. Footprints are typically larger over water, with 90% of the
 377 flux signal contained within 5 km of the measurement point.

378 2.4.4 Flux disaggregation

379 The observed flux contains contributions from the fluxes of different land classes
 380 contained within the flux footprint. To derive the mean flux for each vegetation type over a set of
 381 flux observations (e.g., flux leg, single flight, or period of deployment), we used the method
 382 described in Hannun et al. (2020). This method utilizes the Disaggregation combining Footprint
 383 analysis and Multivariate Regression (DFMR) technique of Hutjes et al. (2010). Here the
 384 observed flux is treated as a linear combination of component fluxes from each land class within
 385 the footprint, such that:

$$386 \quad F_{obs} = \sum_{k=1}^n C_k F_k \quad (6)$$

387 C_k is the fractional contribution of the k^{th} land class to the flux footprint, and F_k is the average
 388 flux from the corresponding land class over the observation period. C_k for each 1 Hz flux
 389 observation was determined by overlaying the footprint function onto a gridded map of land
 390 cover (Fig 3, Fig 4) and weighting by the contribution of each grid cell to the observed flux
 391 (areas closer to the measurement point contribute more heavily to the measurement). F_k was
 392 calculated via multilinear regression of F_{obs} versus C_k for each land class that constituted more
 393 than 25% of the flux footprint over more than 10 linear km of cumulative (but not necessarily
 394 consecutive) observations. This criterion was selected to ensure sufficient sampling of each land
 395 class during the observation period. The regions that met this criterion were mangrove forests,
 396 mangrove scrub, mangrove shrubland, ghost forest, salt marsh, freshwater marsh, swamp shrub,
 397 swamp scrub, swamp forest, and upland forest.

398 Uncertainty in mean fluxes for each land class was calculated as the statistical uncertainty
 399 in the regression. Random and systematic errors, as well as the calculated divergence correction
 400 (summed in quadrature to yield the total uncertainty) for each flux observation were also
 401 propagated through the regression analysis. We do not include uncertainties in the land surface
 402 data or the footprint analysis, as we expect these to be comparatively small (Hannun et al., 2020).

403 Disaggregation of fluxes from additional categorical land data were computed using the
 404 same method as for vegetation data. Continuous numerical land cover data, such as NDVI, do
 405 not require multivariate regression to disaggregate fluxes. After superimposing the footprint
 406 function onto the geographical data set, the footprint weighted average of the land cover data can
 407 simply be calculated at each 1 Hz observation in the same manner as for fractional land class
 408 contributions (e.g., C_k).

409 3 Results and Discussion

410 3.1 Heterogenous CWT-derived Fluxes

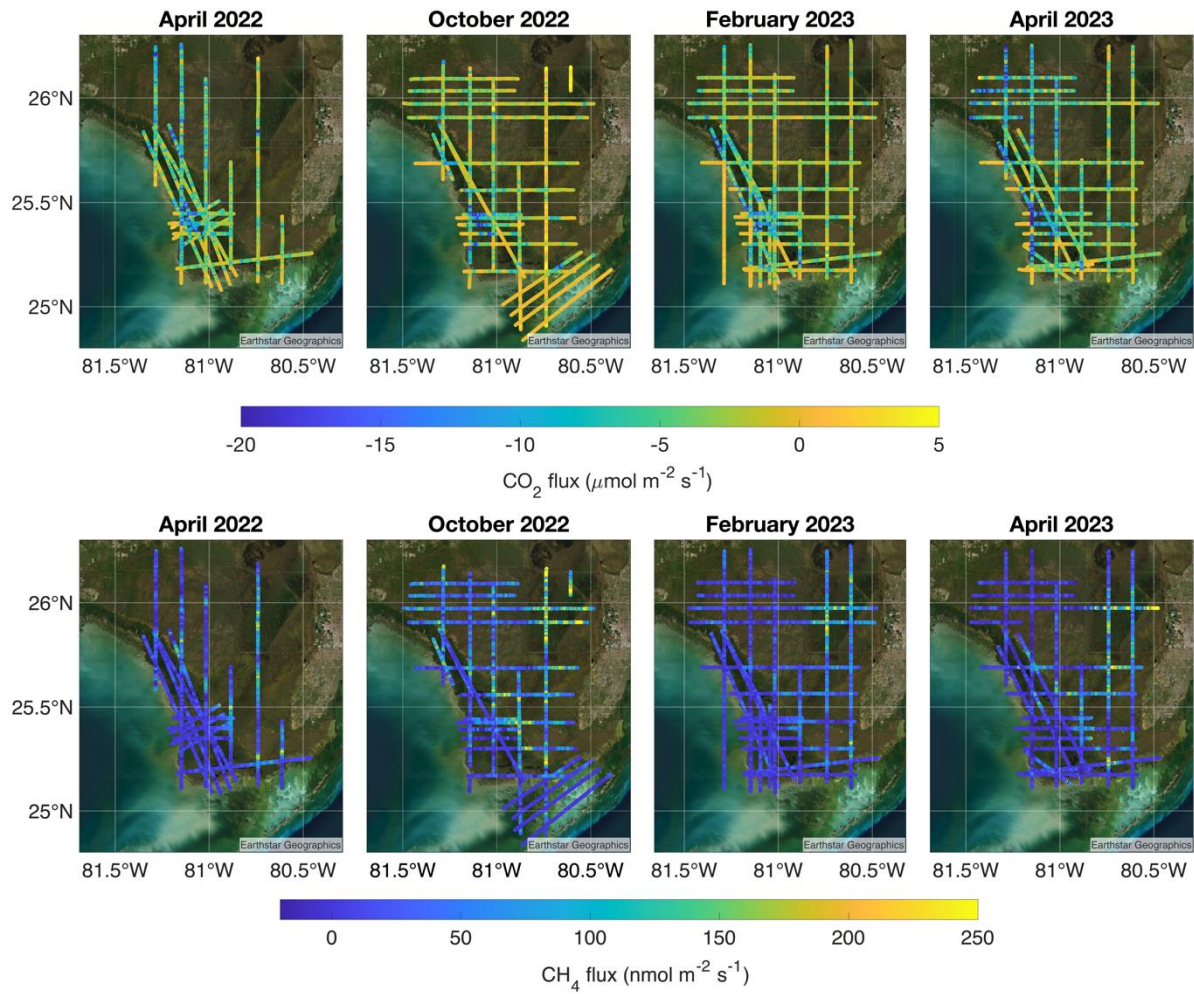


Figure 5: Spatial distribution of (top) CO₂ and (bottom) CH₄ 1 km averaged fluxes over flight legs below 100 m altitude for all seasons. Here negative fluxes denote uptake and positive fluxes represent emission. Flux rates are color coded to scale below maps. Larger CO₂ uptake fluxes appear as darker colors, while larger CH₄ emissions appear as brighter colors

411 The airborne CWT derived fluxes measured below 100 m flight altitude are shown in
 412 Figure 5. Negative and positive fluxes represent uptake and emission by the surface,
 413 respectively. These fluxes provide a measurement of the net ecosystem exchange (NEE) of CO₂
 414 and CH₄, as the aircraft samples the net canopy exchange (photosynthetic uptake, respiration,
 415 and storage) of carbon. Downward (i.e., uptake) CO₂ fluxes are largest (less than -15 μmol m⁻² s⁻¹)
 416 during all flight periods over mangrove forests in the southwest portion of the flight domain,
 417 near 25°30' N and 81° W. During both April deployments, high rates of CO₂ uptake were also
 418 observed in the northwest quadrant over the swamp and upland forests of BCNP.

419 Methane fluxes also demonstrate significant spatial heterogeneity during all deployment
 420 periods. The largest methane fluxes (greater than 200 nmol m⁻² s⁻¹) occur in the northeast portion
 421 of the flight domain over freshwater marshes. High CH₄ emissions also appear in a band just
 422 inland of the west coast in the transition region between mangroves and marshlands (Fig 3, Fig
 423 5).

424 3.2 Drivers of CO₂ uptake and CH₄ emission

425 3.2.1 Vegetation class

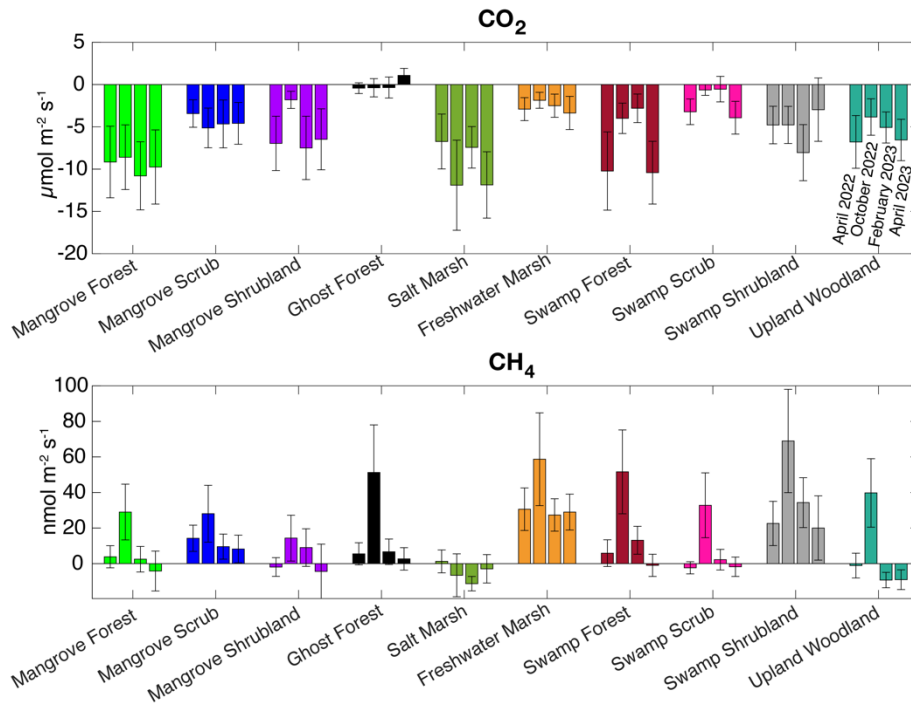


Figure 6: CO₂ and CH₄ fluxes disaggregated by land class for all flights during April 2022, October 2022, February 2023, and April 2023. Fluxes are grouped by vegetation coverage. Error bars represent $\pm 1\sigma$ uncertainty in the component flux, which includes systematic, random, and divergence flux uncertainties propagated through the regression analysis, in addition to the regression residuals, which also reflect the variability in carbon fluxes for each vegetation regime.

426 Figure 6 shows that CO₂ and CH₄ fluxes clearly and consistently vary according to the
427 underlying vegetation type. In some cases, there is also an apparent seasonality in the fluxes.
428 Disaggregated fluxes demonstrate that the largest fluxes of CO₂ uptake were observed for
429 mangrove forests, salt marshes and swamp forests. The greatest CH₄ emissions were consistently
430 measured over freshwater marshes and swamp shrublands. Below we discuss in detail the
431 patterns in observed carbon exchange for mangrove, salt marsh, freshwater wetlands, and upland
432 ecosystems.

433

434 *Mangroves*

435 Mangrove forest CO₂ fluxes did not exhibit much variation over the different sampling
436 months, with the largest average uptake rate of $-11 \pm 4 \mu\text{mol m}^{-2} \text{s}^{-1}$ observed during February
437 2023. These fluxes are consistent with the range of -5 to $-18 \mu\text{mol m}^{-2} \text{s}^{-1}$ uptake observed in the
438 Yucatan during 2017—2018 from an eddy-flux tower (Alvarado-Barrientos et al., 2021). Large
439 peak daily fluxes of -13 to $-20 \mu\text{mol m}^{-2} \text{s}^{-1}$ and -17.1 to $-19.9 \mu\text{mol m}^{-2} \text{s}^{-1}$ have been observed in
440 coastal southeastern China (Zhu et al., 2021) and near Hong Kong (Liu and Lai 2019),
441 respectively. Weak seasonality of CO₂ fluxes was also observed in both other regions. We
442 regularly observed fluxes of -17 to $-22 \mu\text{mol m}^{-2} \text{s}^{-1}$ near the SRS-6 tower site in southwestern
443 ENP, where previous studies have reported the highest mangrove above-ground biomass and
444 productivity (Castañeda-Moya et al., 2013; Danielson et al., 2017; Rivera-Monroy et al., 2019)
445 (Fig. 5, Fig S17, Fig S18). Barr et al. (2010) reported peak uptake values between -15 and -25
446 $\mu\text{mol m}^{-2} \text{s}^{-1}$ at the SRS-6 tower site prior to Hurricane Wilma in 2005, suggesting the strong
447 carbon sink capacity of these riverine mangroves. Our smaller average midday CO₂ fluxes
448 compared with other regions of mangroves may in part be due to lasting effects of past
449 hurricanes. Hurricane Andrew in 1992 had devastating impacts on mangrove forests (Smith et
450 al., 2005). Although trees recovered, canopy heights are still lower in some areas than pre-
451 Andrew levels. High winds and large storm surges from Hurricane Irma in 2017 also created
452 ghost forests and caused additional canopy height loss (Lagomasino et al., 2021).

453 Average mangrove shrub CO₂ fluxes were very similar to the $-8.11 \mu\text{mol m}^{-2} \text{s}^{-1}$ fluxes
454 measured for mangroves of similar heights and speciation in Baja California Sur, Mexico
455 (Zulueta et al., 2013). Lesser average uptake of -3 to $-5 \mu\text{mol m}^{-2} \text{s}^{-1}$ was measured for mangrove
456 scrub systems, which have a lower average canopy height (< 2 m) compared to mangrove
457 shrublands (2-5 m) and forests (>5 m). The mangrove shrublands exhibit greatly reduced CO₂
458 uptake during October 2022. The cause of this reduction in productivity is unclear but may be
459 due to either increased freshwater inundation during the wet season, or differences in flight paths
460 and conditions that led to more limited sampling of mangrove shrublands during October 2022.
461 If the first explanation was the cause, we would likely have also seen an effect in mangrove
462 scrub fluxes. Mangrove shrublands contributed half as much to the total cumulative flux
463 footprints during October 2022 as the other deployment periods, making it difficult to rule out
464 sampling bias. A single flight on October 17, 2022, comprised half of the sampled mangrove
465 shrublands (Table S1). This particular flight resulted in a uniquely low estimate for the CO₂
466 fluxes for mangrove shrublands (Table S2). If this flight were omitted from the October 2022
467 mangrove shrubland disaggregation calculation, the average CO₂ for this vegetation class during

468 October 2022 would be $-8 \pm 4 \mu\text{mol m}^{-2} \text{s}^{-1}$, similar to the estimates for the other sampling
469 periods.

470 Measured CH_4 fluxes likely integrate contributions of water-atmosphere fluxes from
471 mangrove tidal creeks and sediment-atmosphere fluxes. Insignificant CH_4 emissions were
472 measured for mangrove forests except during the October 2022 (end of wet season) period of
473 high inundation, when average CH_4 fluxes were $29 \pm 16 \text{ nmol m}^{-2} \text{s}^{-1}$ (Fig. 6, lower panel).
474 Fluxes from mangrove scrubs and shrublands were also higher in October 2022, though these
475 areas tended to have larger dry-season CH_4 fluxes, ranging from 8 to $14 \text{ nmol m}^{-2} \text{s}^{-1}$ among
476 mangrove scrub and from -4 to $9 \text{ nmol m}^{-2} \text{s}^{-1}$ for mangrove shrublands. Rosentreter et al.
477 (2018a) observed a similar range of $0.5\text{--}12 \text{ nmol m}^{-2} \text{s}^{-1}$ ($40\text{--}1000 \mu\text{mol m}^{-2} \text{d}^{-1}$) water-
478 atmosphere exchange from flux chambers at three sites in Australia, with the highest fluxes
479 during the wet season. Much larger fluxes from mangrove soils of $110 \pm 180 \text{ nmol m}^{-2} \text{s}^{-1}$ ($150 \pm$
480 $250 \text{ mg m}^{-2} \text{d}^{-1}$) were observed during the wet season in India (Jha et al., 2014), and CH_4 fluxes
481 from soils ranged from 0.02 to $88 \text{ nmol m}^{-2} \text{s}^{-1}$ at four mangrove sites in Taiwan (Lin et al.,
482 2020). There is a large variability of CH_4 emissions from mangrove waters and soils that have
483 been reported, with an estimated global average of $3.9 \pm 1.2 \text{ nmol m}^{-2} \text{s}^{-1}$ ($339 \pm 106 \mu\text{mol m}^{-2} \text{d}^{-1}$)
484 (Rosentreter et al., 2021).

485 Mangrove ghost forests predictably did not take up CO_2 . In these areas there had been a
486 high tree mortality rate and massive defoliation post-Irma, without signs of recovery three years
487 post-storm (Xiong et al., 2022). CO_2 exchange was not statistically different from zero during the
488 first three deployment periods, but ghost forests served as a small source of CO_2 ($1.1 \pm 0.8 \mu\text{mol}$
489 $\text{m}^{-2} \text{s}^{-1}$) during April 2023. It should be noted that during this deployment period we more heavily
490 targeted ghost forests, particularly during the flight on April 18, 2023 (Table S1). Ghost forests
491 were a methane source across all deployment months, particularly during October 2022 when we
492 observed an average emission rate of $51 \pm 27 \text{ nmol m}^{-2} \text{s}^{-1}$. During this period ghost forests
493 emitted more CH_4 than any of the intact mangrove areas. Higher CH_4 emissions and eliminated
494 CO_2 uptake from ghost forests highlights the importance of mangrove preservation for mitigation
495 of carbon emissions, and the potential for additional GHG emissions as hurricanes and coastal
496 development continue to threaten mangrove communities globally. This is particularly
497 significant in south Florida mangrove communities, given the high tropical storm recurrence
498 frequency in this region and the significant impacts of past hurricanes on forest structure and
499 productivity (Danielson et al., 2017; Rivera-Monroy et al., 2019; Lagomasino et al., 2021; Xiong
500 et al., 2022; Chavez et al., 2023).

501 *Saltwater Marshes*

502 Average daily NEE for saltwater marshes ranged from -6 to $-12 \mu\text{mol m}^{-2} \text{s}^{-1}$ with no
503 statistically significant seasonality. Similar fluxes of $-6.7 \pm 5.5 \mu\text{mol m}^{-2} \text{s}^{-1}$ (winter—spring) and
504 $-7.9 \pm 6.4 \mu\text{mol m}^{-2} \text{s}^{-1}$ were observed from an eddy-covariance tower in a tidal salt marsh in
505 Brazil (Souza et al., 2022). An NEE range of -5 to $-15 \mu\text{mol m}^{-2} \text{s}^{-1}$ was also recorded at a
506 subtropical estuarine marsh in Taiwan (Lee et al., 2015).

507 CH_4 fluxes from saltwater marshes were insignificant, except during February 2023,
508 when CH_4 fluxes were $-11 \pm 4 \text{ nmol m}^{-2} \text{s}^{-1}$. Saline marshes typically emit less CH_4 than
509 freshwater marshes because sulfate reduction dominates over methanogenesis during

510 decomposition of organic matter (Bartlett et al., 1987). Low methane emission fluxes of $0.08 \pm$
 511 $0.02 \text{ nmol m}^{-2} \text{ s}^{-1}$ ($0.04 \pm 0.01 \text{ g m}^{-2} \text{ yr}^{-1}$) have also been observed in a tropical region of
 512 northwest Australia (Iram et al., 2021). In general, a large range of methane emissions from salt
 513 marshes has been observed globally (-1 to $1090 \text{ nmol m}^{-2} \text{ s}^{-1}$, -92 to $94,000 \text{ } \mu\text{mol m}^{-2} \text{ d}^{-1}$), with an
 514 estimated average of $2.6 \text{ nmol m}^{-2} \text{ s}^{-1}$ ($224 \text{ } \mu\text{mol m}^{-2} \text{ d}^{-1}$) (Al-Haj and Fulweiler, 2020).

515 The reason for the different net CH_4 and CO_2 fluxes during each deployment is not
 516 immediately obvious. Methane and CO_2 soil respiration fluxes in salt marshes are known to be
 517 influenced by tidal cycles (Kristensen et al., 2008; Rosentreter et al., 2018c; Iram et al., 2021)
 518 and it is possible that our flight data were skewed by sampling different tidal regimes. Methane
 519 uptake due to increased oxidation by methanotrophic bacteria has also been observed during the
 520 dry season of a coastal wetland in China (e.g. Hao et al., 2020). It is possible that abnormally low
 521 rainfall during February 2023 in southwest Florida contributed to the more significantly negative
 522 methane fluxes during this period.

523 *Freshwater Marshes and Swamplands*

524 Freshwater marshes, swamp forests, swamp scrub, and swamp shrublands are all
 525 considered freshwater wetlands. Their different classifications reflect differences in vegetation
 526 composition and distribution, with a higher percentage of tall tree cover for swamp forests and a
 527 higher percentage of grasses in freshwater marshes (Section S3). The Shark River Slough, Taylor
 528 Slough, and several other sloughs that flow through the Big Cypress Swamp connect these areas
 529 with the saltwater tidal wetlands. CO_2 uptake fluxes were relatively low over freshwater marshes
 530 (-2.9 to $-3.6 \text{ } \mu\text{mol m}^{-2} \text{ s}^{-1}$), with a weak seasonality. Similar daily peak fluxes for two freshwater
 531 marsh sites in ENP were observed using chamber measurements in 2008—2009 (Schedlbauer et
 532 al., 2012). The relatively low CO_2 fluxes for freshwater marshes are likely due to the lower LAI
 533 and biomass for grasses than for regions containing larger shrubs and trees (Fig. 6, Fig S17, Fig
 534 S18). Inundation also plays a significant role in these systems, causing a decline in
 535 photosynthesis with increasing length of flooding (Zhao et al., 2021). CO_2 fluxes in swamp
 536 shrublands were larger than in freshwater marshes, with a weak seasonality. These areas consist
 537 of a variety of evergreen tree species in a matrix of grasses (Supplementary Information Section
 538 S3). Average fluxes to swamp shrublands were more uncertain in April 2023, likely due to less
 539 area sampled than during other deployment periods (Table S1).

540 Many of the freshwater wetland regions of the Everglades, particularly freshwater
 541 marshes and swamp shrublands, contain periphyton mats in the water. These periphyton mats
 542 grow during the wet season and during periods of inundation, when they are active in fixing CO_2
 543 from the atmosphere as calcium carbonate (Schedlbauer et al., 2012). The balance of CO_2 uptake
 544 from plant and periphyton communities, CO_2 emission from soils and waters, and the effect of
 545 inundation on these processes likely drives observed temporal changes in CO_2 exchange.

546 CO_2 fluxes from swamp forests were largest during April 2022 and April 2023 (-10 ± 5
 547 $\text{ } \mu\text{mol m}^{-2} \text{ s}^{-1}$ and $-10 \pm 4 \text{ } \mu\text{mol m}^{-2} \text{ s}^{-1}$, respectively), during the dry- to wet-season transition
 548 period, with much smaller fluxes observed during October 2022 and February 2023 ($-4 \pm 2 \text{ } \mu\text{mol}$
 549 $\text{ m}^{-2} \text{ s}^{-1}$ and $-3 \pm 2 \text{ } \mu\text{mol m}^{-2} \text{ s}^{-1}$, respectively) when the sun was lower and temperatures were
 550 cooler. Similar seasonality can be seen for swamp scrub. Swamp forests and swamp scrub
 551 vegetative regions are dominated by deciduous bald cypress trees (Ruiz et al., 2021). The

552 majority of these conifers were observed to either lack leaves or had brown needles during
553 October and February flights.

554 CH₄ emissions were largest for freshwater marshes and swamp shrublands, with the
555 largest emissions in October 2022 during the tail end of the wet season when soils were
556 inundated. Average October 2022 fluxes for freshwater marshes, swamp forests, swamp scrubs,
557 and swamp shrublands were $59 \pm 26 \text{ nmol m}^{-2} \text{ s}^{-1}$, $52 \pm 24 \text{ nmol m}^{-2} \text{ s}^{-1}$, $33 \pm 18 \text{ nmol m}^{-2} \text{ s}^{-1}$, and
558 $69 \pm 29 \text{ nmol m}^{-2} \text{ s}^{-1}$, respectively. Much larger CH₄ fluxes of 42—1200 nmol m⁻² s⁻¹, (44—1244
559 mg C-CH₄ m⁻² d⁻¹) have been recorded in both marsh and forested wetland areas of Veracruz,
560 Mexico (Marín-Muñiz et al., 2015) and Costa Rica (Nahlik and Mitsch 2011). More comparable
561 CH₄ emission rates of 48—290 nmol m⁻² s⁻¹ (0.05—0.3 g C-CH₄ m⁻² d⁻¹) during periods of
562 inundation, and $2 \pm 1 \text{ nmol m}^{-2} \text{ s}^{-1}$ ($0.002 \pm 0.001 \text{ g C-CH}_4 \text{ m}^{-2} \text{ d}^{-1}$) during dry conditions were
563 recorded from an eddy flux tower in the Pantanal wetland of Brazil (Dalmagro et al., 2019).
564 Recently, Murguia-Flores et al. (2023) identified a median (IQR) CH₄ emission rate for tropical
565 shallow-water inland wetlands of 39.2 (7.1—180.7) nmol m⁻² s⁻¹, or 40.6 (7.4—187.3) g C-CH₄ m⁻²
566 d⁻¹. Our measurements from freshwater wetlands in southern Florida fall within this range and
567 close to the reported median.

568 *Upland Woodlands*

569 Upland woodlands exhibited a moderately high NEE ranging from -4 to -8 μmol m⁻² s⁻¹.
570 A similar range (-6 to 12 μmol m⁻² s⁻¹) of NEE for slash pine plantations in subtropical Australia
571 was also observed across wet and dry seasons (McGowan et al., 2020). This vegetation region
572 also demonstrates a similar but less pronounced seasonal cycle of CO₂ fluxes as swamp forests.
573 Although most of the upland woodlands in this region are dominated by evergreen slash pine,
574 this seasonality may be caused by variations in PAR and by the presence of some semi-
575 deciduous species, such as laurel oaks. It is also possible that the productivity of flood-intolerant
576 upland woodland species was somewhat suppressed during October 2022 at the tail of the wet
577 season when water levels were relatively high (Fig S17). Reduction of NEE for October 2022
578 could have also been driven by increased soil respiration during the wet season when soil
579 moisture was higher (Fig S17), (Orchard and Cook 1983, Hawkes et al., 2016).

580 Methane fluxes from upland woodlands were undetectable in April 2022, and were
581 slightly negative at $-9 \pm 4 \text{ nmol m}^{-2} \text{ s}^{-1}$ and $-9 \pm 5 \text{ nmol m}^{-2} \text{ s}^{-1}$ for February 2023 and April 2023,
582 respectively. Similar negative fluxes have also been observed during the dry season in tropical
583 upland forests in Costa Rica (Nahlik and Mitsch, 2011). In contrast, a large positive flux of
584 methane ($40 \pm 19 \text{ nmol m}^{-2} \text{ s}^{-1}$) was observed during October 2022. Wet season methane
585 emissions have been observed in upland regions of tropical and subtropical regions elsewhere,
586 when upland forests and woodlands can switch from being a methane sink to a methane source
587 (Megonigol and Guenther, 2008).

588 3.2.2 Other surface properties

589 Within each vegetation land classification, there still exists substantial surface
590 heterogeneity. For example, comparing the extent of mangrove forests (Fig. 2) with the maps of
591 observed fluxes (Fig 5), it is apparent that this ecosystem exhibits a range of midday fluxes, even
592 within the same month. The interquartile range of CO₂ fluxes observed where the footprint

593 consists of 80% mangrove forest is -15.1 to $-6.5 \mu\text{mol m}^2\text{s}^{-1}$ during April 2022. Similarly, the
 594 interquartile range of CH_4 fluxes observed where the footprint consists of 80% freshwater marsh
 595 is 13 to $73 \text{ nmol m}^2 \text{ s}^{-1}$ during April 2022. Vegetation type alone explains 35 - 53% of variability
 596 in observed fluxes (Fig S16). Variability in the underlying drivers of CO_2 and CH_4 exchange
 597 within an ecosystem type also influences heterogeneity in fluxes. For example, the range of LAI
 598 for footprints containing 80% or more mangrove forests in April 2022 was 1.9 to $6.3 \text{ m}^2/\text{m}^2$ and
 599 the range of canopy heights was 5—20 m. For footprints containing 80% or more freshwater
 600 marsh in October 2022, the range of water depths was 6—97 cm.

Table 1: Spearman's correlation coefficients for GHG fluxes and surface properties.

Data set	CO_2 all	CO_2 mangrove ^{a,b}	CH_4 all	CH_4 freshwater marsh ^a
<i>LAI</i>	-0.52	-0.36	-0.16	-0.02
<i>FPAR</i>	-0.52	-0.39	-0.07	0.07
<i>EVI</i>	-0.51	-0.51	-0.23	-0.17
<i>NDVI</i>	-0.46	-0.51	-0.14	0.06
<i>Canopy Height</i>	-0.35	-0.54	-0.33	-0.11
<i>AGBM</i>	-0.35	-0.54	-0.27	-0.13
<i>Soil moisture</i>	0.17	0.05	0.27	0.16
<i>water depth</i>	0.18	-0.33	0.53	0.44
<i>PAR</i>	-0.14	0.03	-0.10	-0.11
<i>VPD</i>	-0.32	-0.12	-0.02	-0.07
<i>T</i>	-0.06	0.02	-0.05	0.13
<i>RH</i>	0.25	0.12	-0.02	0.15

a. Considering footprints consisting of more than 80% of the given land type.

b. All mangrove ecosystems (forest, shrubland, scrub) are combined.

601 Spearman's correlation coefficients between 1 km averaged GHG fluxes and a variety of
 602 surface and atmospheric variables are shown in Table 1. For surface data sets (LAI, FPAR, EVI,
 603 NDVI, Canopy Height, AGBM, soil moisture, and water depth) correlation coefficients are
 604 calculated between GHG fluxes and footprint weighted variables. Vapor pressure deficit (VPD),
 605 temperature (T), and relative humidity (RH) are based on airborne temperature and water vapor
 606 measurements. Photosynthetically active radiation (PAR) was estimated from the NOAA High-
 607 Resolution Rapid Refresh (HRRR) Model product at 3 km resolution interpolated to the 1 km
 608 averaged flight tracks. Spearman's correlation coefficients were used over Pearson's coefficients
 609 because many of the relationships between the environmental and surface variables are non-
 610 linear (Fig. 7, Fig 8).

611 The strongest predictors of CO_2 fluxes for all flux data were LAI and FPAR (Table 1, Fig
 612 7). However, within mangrove ecosystems (forest, shrublands, and scrub), canopy height and
 613 above ground biomass had the most robust relationship with CO_2 fluxes. In contrast, CH_4 fluxes
 614 over all flight tracks and over freshwater marshes both correlate best with EDEN water depth
 615 (Table 1, Fig 8). The largest CH_4 fluxes and EDEN water depths were over water management

616 regions outside of ENP or BCNP boundaries (Fig 3, Fig 5, Fig S17). The influence of water on
 617 the methane emissions is not surprising, as numerous studies have observed larger methane
 618 emissions in coastal wetlands during the wet season when soils are inundated and conditions in
 619 the soil become more anaerobic and ideal for methanogenesis (e.g. Nahlik and Mitsch 2011;
 620 Beringer et al., 2013; Marín-Muñiz et al., 2015; Dalmagro et al., 2019; Hondula et al., 2021).
 621 This relationship confirms that higher CH₄ fluxes during October 2022 were likely due to
 622 inundation. This flight period occurred following Hurricane Ian. Analysis of EDEN water data
 623 sets since 2002 suggests that water levels were slightly elevated relative to the October average,
 624 but comparable to many other years on record (Fig S19).

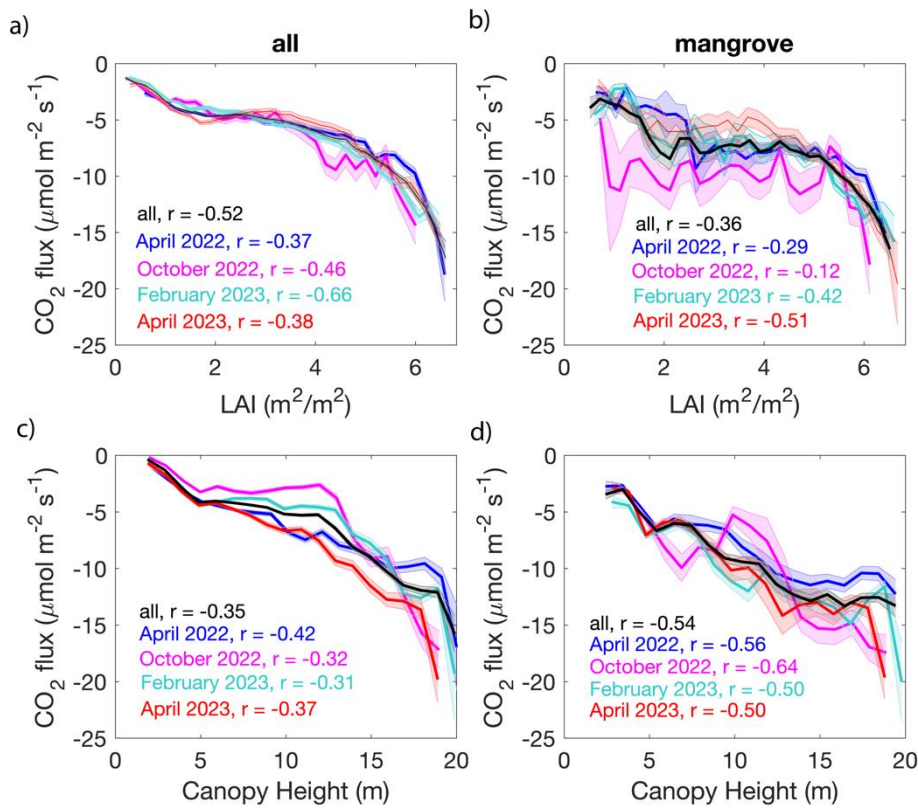


Figure 7: Relationships between CO₂ flux and leaf area index (LAI) (**a, b**) and between CO₂ flux and Canopy Height (**c, d**) for all 10 second averaged data (**a, c**), and for data where footprints were comprised of 80% mangroves (mangrove forests, mangrove shrublands, and mangrove scrubs) (**b, d**). CO₂ data are averaged over 0.25 m² m⁻² LAI bins or 2 m canopy height bins. Solid black, blue, magenta, turquoise, and red lines are the average for all flights, April 2022, October 2022, February 2023, and April 2023, respectively. Shaded areas are the 95% confidence interval of the mean.

625 Interestingly, we observe a slightly negative relationship between VPD and CO₂ flux.
 626 This is likely both due to the generally high humidity and water availability in the region (50—
 627 90%) and because VPD was higher during the April months when there was greater sunlight

628 availability and the deciduous bald cypress trees were green. Similar relationships between VPD
 629 and mangrove NEE have also been reported for mangroves in the Yucatan (Alvarado-Barrientos
 630 et al., 2020).

631 Some relationships between fluxes and environmental variables likely come about
 632 because of redundant and non-causal correlations. For example, the negative relationship
 633 between canopy height and CH₄ fluxes, are likely due to correlations between surface variables.
 634 In this case, greater canopy height likely does not cause lower CH₄ emissions, but areas with
 635 greater canopy heights are often mangrove forests and areas with less surface water extent where
 636 there are low CH₄ emissions. Many of the variables tested, such as EVI, NDVI, Canopy Height,
 637 LAI, and AGBM also co-vary with each other.

638 The relationships between remotely sensed vegetation and soil properties and carbon
 639 fluxes demonstrate the potential predictive power of remote sensing for greenhouse gas fluxes.
 640 Incorporation of remotely sensed data sets into a predictive machine learning model of southern
 641 Florida CO₂ and CH₄ fluxes is a part of ongoing work.

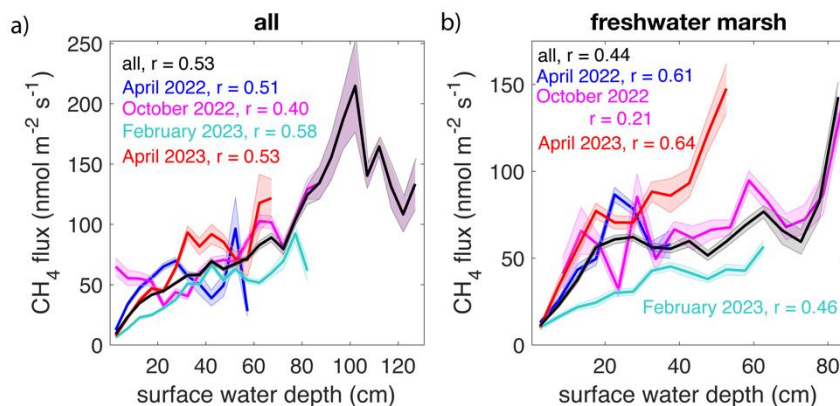


Figure 8: Relationships between CH₄ flux and EDEN surface water depth all 10 second averaged data (a), and for data where footprints were comprised of 80% freshwater marsh (b). CH₄ fluxes are averaged over water depth in 5 cm bins. Solid black, blue, magenta, turquoise, and red lines are the average for all flights, April 2022, October 2022, February 2023, and April 2023, respectively. Shaded areas are 95% confidence intervals. All 10-second averaged data include areas outside of the national park boundaries where vegetation data area available.

642

643 3.3 Flux tower comparisons

644 Comparison of airborne fluxes to EC flux tower measurements requires careful
 645 consideration of flux footprints (Hannun et al., 2020). Only one flight had a flux footprint that
 646 directly overlapped with the mangrove forest tower site (SRS-6) while that tower site was active,
 647 and measurements only overlapped for several seconds, making a direct comparison with the
 648 flux towers impossible. Indirect comparison of airborne and EC tower fluxes is complicated by
 649 surface variability and resulting heterogeneity of fluxes. Each airborne flux footprint typically

650 consisted of several vegetation types and a further range of surface properties (LAI, canopy
 651 heights, soil moisture, surface water extent, etc.). In contrast, the EC tower footprints typically
 652 covered only single ecosystem type with greater homogeneity.

653 We indirectly compare the average monthly fluxes of CH_4 and CO_2 from eddy covariance
 654 tower ground sites (when available) to airborne flux measurements with footprints consisting
 655 primarily of similar surface properties as the ground sites. Airborne CO_2 and CH_4 fluxes were
 656 averaged over all flight days during a given month after selecting for data that met certain criteria
 657 for comparison with the EC tower. For CH_4 flux comparisons with SRS-2 and TS/Ph-1, airborne
 658 data were filtered to only include points where freshwater marsh constituted more than 80% of
 659 the footprint and the footprint weighted average water depth was within 10 cm of the EC tower
 660 for the given month (Table S6). For SRS-6 comparison, airborne fluxes were included in the
 661 average if footprints contained more than 80% mangrove forest. Airborne CO_2 fluxes were
 662 averaged during each flight day where footprints constituted over 80% of the EC tower land
 663 classification and had a footprint weighted LAI within $1 \text{ m}^2/\text{m}^2$ of the EC tower footprint LAI for
 664 the given month (Table S7). EC tower fluxes were averaged for all available data during a given
 665 month from 10:00—17:00 local time (LT).

666 Comparisons indicate relatively good agreement between EC flux tower and airborne
 667 flux measurements (Fig. 9). These comparisons provide a validation of our airborne CWT fluxes,
 668 as well as confirm that surface water extent, LAI, and vegetation class indeed capture much of
 669 the observed variability in carbon exchange. Tower comparisons with latent heat (LE) and
 670 sensible heat (H) are discussed in Supplementary Information section S4 and Figures S6-S8.

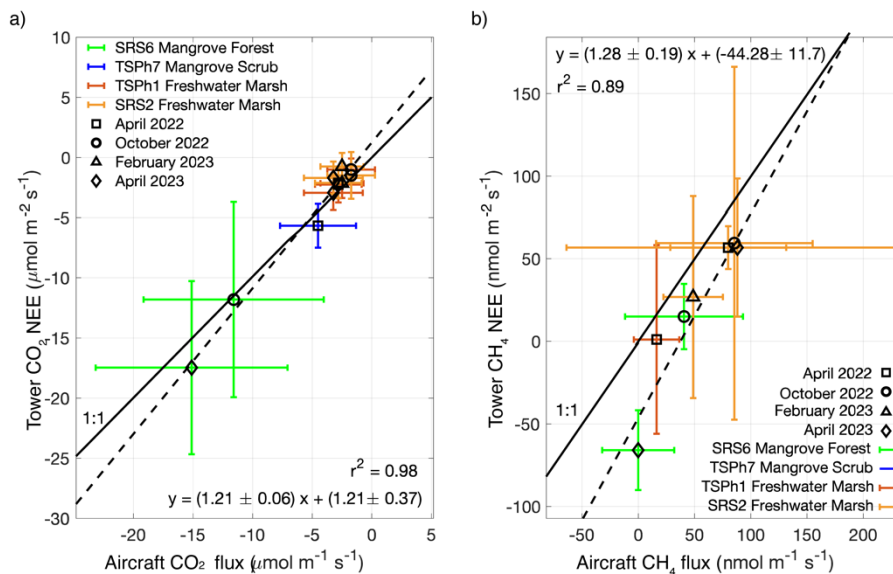


Figure 9: Comparison of EC fluxes from flux tower sites with airborne fluxes measured from the King Air for a) CO_2 and b) CH_4 . EC tower CH_4 and CO_2 NEE (flux – storage) for a given month were averaged over all available data between 10:00 and 16:00 LT. Airborne CH_4 fluxes were averaged over all flight days for data with the same vegetation class and surface water as the EC tower. Airborne CO_2 fluxes were averaged during each flight day after filtering data for the same vegetation class and LAI as the EC tower. EC towers SRS6, SRS2, TSPH1, and TSPH7 sample mangrove forest, freshwater marsh, freshwater marsh, and mangrove scrub, respectively. Error bars are one standard deviation. The dashed line is the 1:1 line.

671

672 3.4. Net carbon fluxes

673

674 The balance between CH₄ emissions and CO₂ uptake partially determines the impact of
 675 wetland ecosystems on carbon sequestration and climate change mitigation. To estimate the net
 676 impact of the entire Everglades region on carbon exchange during our sampling periods, we first
 677 scaled CH₄ fluxes by their CO₂ equivalent global warming potential (GWP) using a factor of
 678 27.9 g CH₄/g CO₂ in accordance with the latest IPCC report (Forster et al., 2021) and then
 679 calculated the net CO₂ equivalent exchange rate and the fraction of total CO₂ uptake that is
 680 offset by CH₄ emissions for each vegetation region based on disaggregated fluxes. These values
 681 were then scaled by the total area of each vegetation region adequately sampled in ENP and
 682 BCNP (Fig. S20, Fig. S21). During daytime sampling periods, the 6,237 km² area of south
 683 Florida represented by the sampled land classes has a total CO₂ equivalent exchange rate of -5.3
 684 ± 2.6 to -2.7 ± 1.5 Gg CO₂ hr⁻¹, with CH₄ emissions offsetting CO₂ by $3 \pm 1\%$ to $14 \pm 4\%$,
 685 depending on the month. The largest CH₄ emissions relative to CO₂ uptake occurred during the
 686 October 2022 deployment (Fig. S21). However, midday airborne flux measurements do not
 687 include nighttime CO₂ respiration which is required for an estimate of daily carbon exchange.

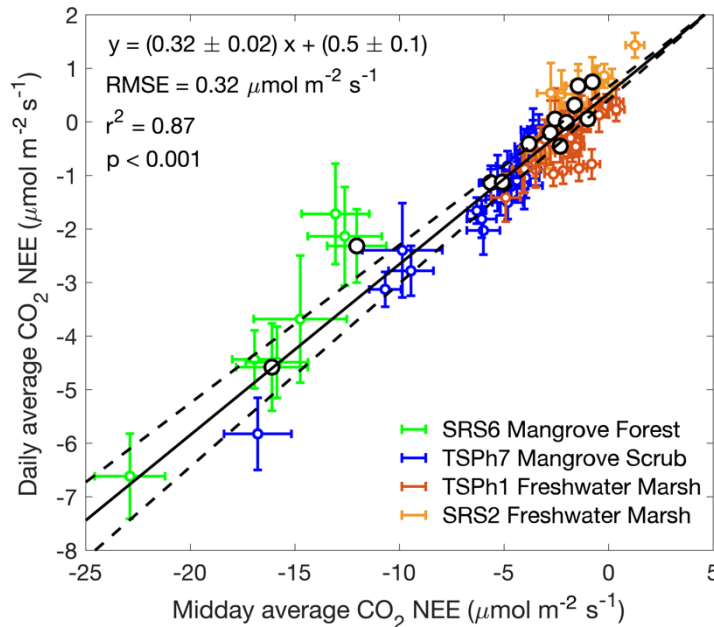


Figure 10: Linear fit of daily integrated net ecosystem exchange (NEE) and the integrated daytime NEE between LT 10:00 and 17:00 for all tower sites in the flight domain. Each marker represents a monthly average from data available between 2020 and 2023. Larger black markers are monthly averages for the months of BlueFlux flights. The line of best fit and the 95% confidence interval are solid and dotted lines, respectively. Error bars are 1σ .

688

689 Tower flux observations constrain the diurnal cycle of carbon exchange in several
 690 locations. We use this diurnal temporal information from the Everglades tower network to
 691 extrapolate to total daily carbon exchange in ENP and BCNP as in Hannun et al. (2020) (Figure
 692 S22). The tower sites in the BlueFlux/FCE LTER domain are located in three different
 693 vegetation regions that represent the three dominant vegetation types, including tall riverine
 694 mangrove forests (SRS-6), scrub mangroves (TS/Ph-7), and freshwater marshes (SRS-2 and
 695 TS/Ph-1). These tower sites demonstrate a linear relationship between the total CO₂ NEE
 696 between LT 10:00 and 17:00 and the total daily integrated NEE (Fig. 10). A similar relationship
 697 was also derived for EC tower sites in the mid-Atlantic region (Hannun et al., 2020). This
 698 relationship is used to scale the CO₂ fluxes measured by CARAFE during LT 10:00—17:00 and
 699 provide an estimate of the total daily carbon exchange. The domain of swamp forests, swamp
 700 scrubs, and upland woodlands were outside the FCE LTER study area. However, chamber
 701 experiments conducted in BCNP during 2012—2014 measured average CO₂ NEE of -108 ± 5 g
 702 C m⁻² month⁻¹, -48 ± 3 g C m⁻² month⁻¹, and -68 ± 5 g C m⁻² month⁻¹ during April months at a
 703 cypress swamp (swamp forest), dwarf cypress (swamp scrub), and pine upland (upland
 704 woodland) site, respectively (Shoemaker et al., 2015). We obtain slightly lower average
 705 estimates for these vegetation areas during our April deployments of -85 ± 40 g C m⁻² month⁻¹, -

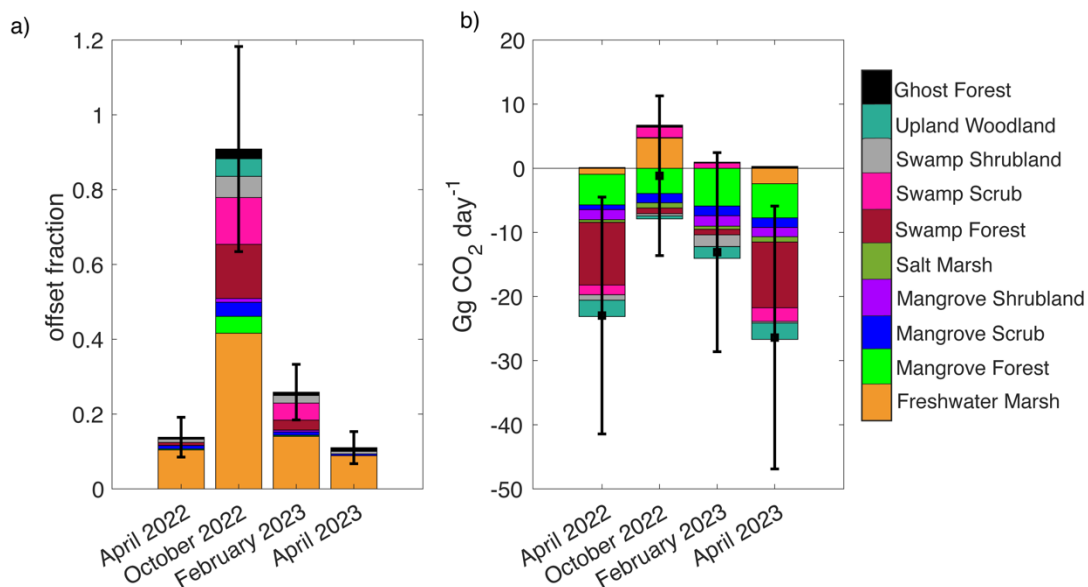


Figure 11: (a) GWP-scaled CH₄ emissions as a fraction of the CO₂ uptake for each month across the BlueFlux experimental domain. Colors indicate the contribution of each ecosystem classification. CH₄ offset fractions are weighted by the area of each ecosystem type. (b) Average daily net CO₂ equivalent uptake for each deployment period, calculated as the sum of CO₂ and GWP-scaled CH₄ fluxes. Total daily CO₂ fluxes were calculated by from the daytime airborne measurements using the linear fit of daily integrated NEE and daytime NEE from Figure 10. CH₄ fluxes were assumed to be constant throughout the day so average disaggregated CH₄ fluxes for each deployment period were scaled by 24 hours. Ecosystem contributions are scaled by area. Error bars are 1σ .

706 $16 \pm 10 \text{ g C m}^{-2} \text{ month}^{-1}$, and $-51 \pm 30 \text{ g C m}^{-2} \text{ month}^{-1}$, respectively, when scaling using the
707 relationship derived in Figure 10.

708 The CH_4 average midday flux measured by the tower sites was not significantly different
709 from the daily average (Figure S23). Thus, CH_4 fluxes are treated as constant throughout the day
710 and average midday CH_4 fluxes were assumed to be representative of daily averaged fluxes.

711 Figure 11 shows the resulting daily CH_4 offsets to CO_2 uptake and net daily CO_2
712 equivalent exchange for each deployment period across ENP and BCNP. CH_4 emissions relative
713 to CO_2 uptake are lowest during April 2023, with CH_4 emissions offsetting $11 \pm 4 \%$ of CO_2
714 uptake and a total net carbon exchange rate of $-26 \pm 20 \text{ Gg CO}_2\text{-eq d}^{-1}$. The largest CH_4 emissions
715 relative to CO_2 uptake are during October 2022, with CH_4 emissions offsetting $91 \pm 27\%$ of CO_2
716 uptake and a net carbon exchange rate of $-1 \pm 12 \text{ Gg CO}_2\text{-eq d}^{-1}$. The largest source of CH_4
717 emissions relative to CO_2 uptake are the freshwater marshes, particularly during the October
718 2022 wet season when they are estimated to provide $5 \text{ Gg CO}_2\text{-eq d}^{-1}$ source of carbon.
719 Mangrove forests contribute a relatively small amount of CH_4 emission and provide the largest
720 net sink of carbon cumulatively across all deployment periods with an average net carbon flux of
721 $-5 \pm 2 \text{ Gg CO}_2\text{-eq d}^{-1}$. Swamp forests provide the largest net carbon sink during the dry/growing
722 season (almost double than that of mangroves), as observed during April 2022 and April 2023.

723 Carbon exchange in southern Florida wetlands exhibits strong seasonality over the
724 measurement period, with the ENP and BCNP region potentially serving as a net source of
725 carbon to the atmosphere during the wet season and periods of high inundation. Mangrove and
726 cypress swamp forests are large atmospheric sinks of carbon for the region, despite their
727 relatively small extents. The importance of cypress swamp forests in CO_2 removal is likely even
728 greater than this study reflects, as we do not have measurements in the summer when leaf area is
729 at a peak.

730 It should also be noted that in tidal wetland regions like the Everglades, the net ecosystem
731 carbon balance is affected by lateral aqueous transport of carbon in addition to NEE (Troxler et
732 al., 2013). Carbon initially taken up in one area may be stored in above and below ground
733 biomass, soils, and sediments, or it may laterally flow from the area of initial uptake to later be
734 reemitted or stored in soils and sediments downstream (Bouillon et al., 2008; Alongi and
735 Mukhopadhyay, 2015; Rosentreter et al., 2018b). Aquatic lateral transport in the Everglades has
736 been estimated to be relatively small ($\sim 10\%$) compared to the NEE of mangrove forests (Troxler
737 et al., 2013). However, freshwater marshes in the Everglades store a substantial amount of
738 carbon ($400\text{-}650 \text{ g C m}^{-2} \text{ yr}^{-1}$), with almost all the carbon input through aqueous lateral transport
739 (Troxler et al., 2013). In this study we discuss the net vertical carbon exchange largely from an
740 atmospheric perspective, but it should not be taken as the complete story of carbon storage in the
741 Everglades.

742 **5 Conclusions**

743 Airborne eddy covariance with continuous wavelet transforms can resolve heterogenous
744 fluxes over a diverse mosaic of ecosystems across the coastal landscape of southern Florida. The
745 largest CO_2 uptake fluxes were observed during April 2022 and 2023 over cypress swamp forests
746 and over mangrove forests during all sampling periods. During the tail-end of the wet season and

747 near maximum water levels (October 2022 campaign), we observed the largest CH₄ emission
748 fluxes from all vegetation types. Across all deployments, we recorded the largest CH₄ fluxes
749 from freshwater marshes and freshwater swamp shrublands. Additionally, we see some evidence
750 for CH₄ uptake during the dry season in salt marshes and upland forests. Upscaling average
751 ecosystem fluxes over the sample domain, we estimate average net CO₂-eq fluxes of -4 ± 3 g
752 CO₂-eq m⁻² d⁻¹ in April and -0.2 ± 2 g CO₂-eq m⁻² d⁻¹ in October (area-integrated rates of -26 ± 20
753 Gg CO₂-eq d⁻¹ and -1 ± 12 Gg CO₂-eq d⁻¹, respectively).

754 Our findings highlight the role of freshwater swamp forests and mangrove forests as
755 extremely productive coastal ecosystems. Rates of CO₂ uptake and CH₄ emission that we
756 observe for these ecosystems fall within the range of observations for mangroves and swamp
757 forests in similar subtropical and tropical regions globally. However, the diversity and
758 vulnerability of these ecosystems necessitates continued ongoing research into the carbon storage
759 potential and the effects of restoration and degradation on the role of swamp and mangrove
760 forests in the global coastal carbon cycle.

761 Combined with landcover information like vegetation type, leaf area, canopy height,
762 vegetation indices, and surface water depth, airborne fluxes can help elucidate the underlying
763 causes of the observed variability in carbon fluxes. In particular, surface water depth in the
764 freshwater wetlands was strongly positively correlated with CH₄ emissions. In a heavily water
765 managed area like southern Florida, policy decisions related to agriculture and hydrology may
766 overlap with greenhouse gas reduction strategies. Moreover, the ongoing large-scale
767 hydrological restoration of the Greater Everglades under the Comprehensive Everglades
768 Restoration Plan (CERP) will likely have significant effects on vegetation dynamics, especially
769 carbon storage and sequestration potential, thereby influencing the role of wetlands in climate
770 change mitigation and adaptation. The relationship between surface water and methane emission
771 in this study relied heavily on the long-term Everglades Depth Estimation Network data set.
772 However, such high-resolution surface information is currently extremely limited globally.
773 Improvements in high resolution remotely sensed soil moisture and surface water data will be
774 critical for ongoing research into relationships between regional hydrology and global methane
775 emissions. Other surface information, such as high-density coastal wetland salinity maps, would
776 also be beneficial to this analysis.

777 This study focused on vegetation types and limited land cover data to demonstrate
778 opportunities for airborne flux observations combined with surface data sets to assess drivers of
779 variability in regional carbon exchange. Future work will combine remotely sensed data sets with
780 airborne and long-term ground-based fluxes to develop historical products and predictive models
781 for CO₂ and CH₄ exchange in southern Florida. Additional work will also quantify local and
782 long-distance lateral fluxes to provide additional constraints on the carbon balance.

783 A limitation of this study is the lack of observations during the peak of the wet season
784 (May-September). During these months temperatures and rainfall tend to be higher, which may
785 impact CO₂ and CH₄ exchange. However, BlueFlux measurements include periods where we
786 would expect both near minimum (April) and near maximum (October) levels of inundation.
787 Daily solar irradiance in April is also within ~5% of the summer maximum. We therefore expect
788 minimal differences in CO₂ fluxes in the summer relative to April due to differences in solar
789 irradiance. Still, additional airborne flux measurements in southern Florida are needed to better

790 constrain seasonality (particularly wet-season fluxes), diurnal cycles, and tidal influences. These
791 efforts would improve the ongoing carbon budget analysis of coastal wetlands in the Everglades
792 region and add an understanding of the carbon sink and source capacity of these ecosystems
793 exposed to increasing impacts of sea-level rise and climate change.

794 The importance of vulnerable coastal wetland ecosystems to the CO₂ and CH₄ global
795 budgets highlights the need for continued and sustained measurements in these regions. Airborne
796 eddy covariance, especially paired with remote-sensing surface information, represents a
797 powerful tool for constraining biogenic carbon cycles.

798 **Acknowledgments**

799 We acknowledge Michael Bonsteel, Irene Romero, Tonya Howington, and Steve Schulze for
800 assistance with National Park permitting. We thank Dynamic Aviation Group Inc. and especially
801 Clay King, Kris Estrep, and Ethan Pearce for their support and flexibility. We gratefully
802 acknowledge the pilots who flew in the BlueFlux mission and were critical for obtaining this
803 data set: Lawrence Grippo, Dustin Hill, Stephen Bielick, Nathan Bierman, Benjamin Powell, and
804 Ryan Kelley. We also thank Bruce Woodcock at Aventech for his assistance in analyzing the
805 winds data from the AIMMS-20 probe. We acknowledge and respect the Indigenous peoples of
806 the Florida Everglades, including the Miccosukee and Seminole Tribes, on whose ancestral lands
807 this research takes place. The BlueFlux mission was supported by the NASA Carbon Monitoring
808 System Solicitation No. NNH20ZDA001N-CMS. ERD was supported by the NASA
809 Postdoctoral Program sponsored by the National Aeronautics and Space Administration (NASA)
810 through a contract with ORAU. Funding for SRS-6, and TS/Ph-7 tower sites is provided by the
811 National Park Service through Cooperative Agreements No. P16AC00032 Task Agreement No.
812 P17AC01282. Towers at SRS-2 and TS/Ph-1 were supported by the National Science
813 Foundation Division of Atmospheric and Geospace Sciences (award 1561139 and 1807533), and
814 the National Science Foundation Graduate Research Fellowship Program (Fellow No.
815 2023348536).

816

817 **Open Research**

818 The airborne data used for all analysis in the study (concentrations, fluxes, meteorology, and aircraft
819 navigational parameters) are openly available at ORNL DAAC via
820 DOI:10.1126/science.216.4547.733 (Delaria et al., 2024).

821

822 **References**

- 823 Adame, M. F., Connolly, R. M., Turschwell, M. P., Lovelock, C. E., Fatoyinbo, T.,
824 Lagomasino, D., Goldberg, L. A., Holdorf, J., Friess, D. A., Sasmito, S. D., Sanderman, J.,
825 Sievers, M., Buelow, C., Kauffman, J. B., Bryan-Brown, D., & Brown, C. J. (2021). Future
826 carbon emissions from global mangrove forest loss. *Global Change Biology*, 27(12).
827 <https://doi.org/10.1111/gcb.15571>
- 828 Al-Haj, A. N., & Fulweiler, R. W. (2020). A synthesis of methane emissions from shallow
829 vegetated coastal ecosystems. In *Global Change Biology* (Vol. 26, Issue 5).
830 <https://doi.org/10.1111/gcb.15046>
- 831 Alongi, D. M., & Mukhopadhyay, S. K. (2015). Contribution of mangroves to coastal carbon
832 cycling in low latitude seas. *Agricultural and Forest Meteorology*, 213.
833 <https://doi.org/10.1016/j.agrformet.2014.10.005>
- 834 Alvarado-Barrientos, M. S., López-Adame, H., Lazcano-Hernández, H. E., Arellano-
835 Verdejo, J., & Hernández-Arana, H. A. (2021). Ecosystem-Atmosphere Exchange of CO₂,
836 Water, and Energy in a Basin Mangrove of the Northeastern Coast of the Yucatan Peninsula.
837 *Journal of Geophysical Research: Biogeosciences*, 126(2).
838 <https://doi.org/10.1029/2020JG005811>
- 839 Barbier, E. B., Hacker, S. D., Kennedy, C., Koch, E. W., Stier, A. C., & Silliman, B. R.
840 (2011). The value of estuarine and coastal ecosystem services. In *Ecological Monographs*
841 (Vol. 81, Issue 2). <https://doi.org/10.1890/10-1510.1>
- 842 Barr, J. G., V. Engel, J. D. Fuentes, J. C. Zieman, T. L. O'Halloran, T. J. Smith III, and G. H.
843 Anderson (2010), Controls on mangrove forest-atmosphere carbon dioxide exchanges in
844 western Everglades National Park, *J. Geophys. Res.*, 115, G02020,
845 doi:10.1029/2009JG001186.
- 846 Barr, J. G., Engel, V., Smith, T. J., & Fuentes, J. D. (2012). Hurricane disturbance and
847 recovery of energy balance, CO₂ fluxes and canopy structure in a mangrove forest of the
848 Florida Everglades. *Agricultural and Forest Meteorology*, 153.
849 <https://doi.org/10.1016/j.agrformet.2011.07.022>

- 850 Bartlett, K. B., Bartlett, D. S., Harriss, R. C., & Sebach, D. I. (1987). Methane emissions
851 along a salt marsh salinity gradient. *Biogeochemistry*, 4(3).
852 <https://doi.org/10.1007/BF02187365>
- 853 Beringer, J., Livesley, S. J., Randle, J., & Hutley, L. B. (2013). Carbon dioxide fluxes
854 dominate the greenhouse gas exchanges of a seasonal wetland in the wet-dry tropics of
855 Northern Australia. *Agricultural and Forest Meteorology*, 182–183.
856 <https://doi.org/10.1016/j.agrformet.2013.06.008>
- 857 Bouillon, S., Borges, A. v., Castañeda-Moya, E., Diele, K., Dittmar, T., Duke, N. C.,
858 Kristensen, E., Lee, S. Y., Marchand, C., Middelburg, J. J., Rivera-Monroy, V. H., Smith, T.
859 J., & Twilley, R. R. (2008). Mangrove production and carbon sinks: A revision of global
860 budget estimates. *Global Biogeochemical Cycles*, 22(2).
861 <https://doi.org/10.1029/2007GB003052>
- 862 Campbell, A. D., Fatoyinbo, L., Goldberg, L., & Lagomasino, D. (2022). Global hotspots of
863 salt marsh change and carbon emissions. *Nature*, 612(7941). [https://doi.org/10.1038/s41586-](https://doi.org/10.1038/s41586-022-05355-z)
864 [022-05355-z](https://doi.org/10.1038/s41586-022-05355-z)
- 865 Castañeda-Moya, E., Twilley, R. R., & Rivera-Monroy, V. H. (2013). Allocation of biomass
866 and net primary productivity of mangrove forests along environmental gradients in the
867 Florida Coastal Everglades, USA. *Forest Ecology and Management*, 307.
868 <https://doi.org/10.1016/j.foreco.2013.07.011>
- 869 Chavez, S., Wdowinski, S., Lagomasino, D., Castañeda-Moya, E., Fatoyinbo, T., Moyer, R.
870 P., & Smoak, J. M. (2023). Estimating Structural Damage to Mangrove Forests Using
871 Airborne Lidar Imagery: Case Study of Damage Induced by the 2017 Hurricane Irma to
872 Mangroves in the Florida Everglades, USA. *Sensors*, 23(15).
873 <https://doi.org/10.3390/s23156669>
- 874 Crawford, T. L., Dobosy, R. J., McMillen, R. T., Vogel, C. A., & Hicks, B. B. (1996). Air-
875 surface exchange measurement in heterogeneous regions: Extending tower observations with
876 spatial structure observed from small aircraft. *Global Change Biology*, 2(3).
877 <https://doi.org/10.1111/j.1365-2486.1996.tb00079.x>
- 878 Danielson, T. M., Rivera-Monroy, V. H., Castañeda-Moya, E., Briceño, H., Travieso, R.,
879 Marx, B. D., Gaiser, E., & Farfán, L. M. (2017). Assessment of Everglades mangrove forest
880 resilience: Implications for above-ground net primary productivity and carbon dynamics.
881 *Forest Ecology and Management*, 404. <https://doi.org/10.1016/j.foreco.2017.08.009>
- 882 Didan, K. (2015). MOD13Q1 MODIS/Terra Vegetation Indices 16-Day L3 Global 250m
883 SIN Grid V006 [Data set]. NASA EOSDIS Land Processes Distributed Active Archive
884 Center. Accessed 2023-09-10 from <https://doi.org/10.5067/MODIS/MOD13Q1.006>
- 885 Dalmagro, H. J., Zanella de Arruda, P. H., Vourlitis, G. L., Lathuilière, M. J., de S.
886 Nogueira, J., Couto, E. G., & Johnson, M. S. (2019). Radiative forcing of methane fluxes
887 offsets net carbon dioxide uptake for a tropical flooded forest. *Global Change Biology*, 25(6).
888 <https://doi.org/10.1111/gcb.14615>

- 889 Delaria, E.R., G.M. Wolfe, R.A. Hannun, K. Blanock, B. Poulter, and K.L. Thornhill. (2024).
890 BlueFlux Airborne Trace Gases, Fluxes, and Mixing Ratios, Southern Florida, 2022-2023.
891 ORNL DAAC, Oak Ridge, Tennessee, USA. <https://doi.org/10.3334/ORNLDAAC/2327>
- 892 Desjardins, R. L., Brach, E. J., Alvo, P., & Schuepp, P. H. (1982). Aircraft monitoring of
893 surface carbon dioxide exchange. *Science*, 216(4547).
894 <https://doi.org/10.1126/science.216.4547.733>
- 895 Donato, D. C., Kauffman, J. B., Murdiyarso, D., Kurnianto, S., Stidham, M., & Kanninen, M.
896 (2011). Mangroves among the most carbon-rich forests in the tropics. *Nature Geoscience*,
897 4(5). <https://doi.org/10.1038/ngeo1123>
- 898 Duarte, C. M. (2017). Reviews and syntheses: Hidden forests, the role of vegetated coastal
899 habitats in the ocean carbon budget. In *Biogeosciences* (Vol. 14, Issue 2).
900 <https://doi.org/10.5194/bg-14-301-2017>
- 901 Dubayah, R., Tang, H., Armston, J., Luthcke, S., Hofton, M., J. B. Blair (2021). GEDI L2B
902 Canopy Cover and Vertical Profile Metrics Data Global Footprint Level V002 [Data set].
903 NASA EOSDIS Land Processes DAAC. Accessed 2022-11-13 from
904 https://doi.org/10.5067/GEDI/GEDI02_B.002.
- 905 Dubayah, R. O., Armston, J., Healey, S. P., Yang, Z., Patterson, P. L., Saarela, S., Stahl, G.,
906 Duncanson, L., Kellner, J. R., Bruening, J., & Pascual, A. (2023). GEDI L4B Gridded
907 Aboveground Biomass Density, Version 2.1. ORNL DAAC, Oak Ridge, Tennessee, USA.
908 <https://doi.org/10.3334/ORNLDAAC/2299>
- 909 Finkelstein, P. L., & Sims, P. F. (2001). Sampling error in eddy correlation flux
910 measurements. *Journal of Geophysical Research Atmospheres*, 106(D4).
911 <https://doi.org/10.1029/2000JD900731>
- 912 Forster, P., T. Storelvmo, K. Armour, W. Collins, J.-L. Dufresne, D. Frame, D.J. Lunt, T.
913 Mauritsen, M.D. Palmer, M. Watanabe, M. Wild, and H. Zhang, (2021). The Earth's Energy
914 Budget, Climate Feedbacks, and Climate Sensitivity. In *Climate Change 2021: The Physical
915 Science Basis. Contribution of Working Group I to the Sixth Assessment Report of the
916 Intergovernmental Panel on Climate Change* [Masson-Delmotte, V., P. Zhai, A. Pirani, S.L.
917 Connors, C. Péan, S. Berger, N. Caud, Y. Chen, L. Goldfarb, M.I. Gomis, M. Huang, K.
918 Leitzell, E. Lonnoy, J.B.R. Matthews, T.K. Maycock, T. Waterfield, O. Yelekçi, R. Yu, and
919 B. Zhou (eds.)]. Cambridge University Press, Cambridge, United Kingdom and New York,
920 NY, USA, pp. 923–1054, doi:10.1017/9781009157896.009.
- 921 Friedlingstein, P., O'sullivan, M., Jones, M. W., Andrew, R. M., Gregor, L., Hauck, J., le
922 Quéré, C., Luijkx, I. T., Olsen, A., Peters, G. P., Peters, W., Pongratz, J., Schwingshackl, C.,
923 Sitch, S., Canadell, J. G., Ciais, P., Jackson, R. B., Alin, S. R., Alkama, R., ... Zheng, B.
924 (2022). Global Carbon Budget 2022. *Earth System Science Data*, 14(11).
925 <https://doi.org/10.5194/essd-14-4811-2022>
- 926 Gaubert, B., Stephens, B. B., Baker, D. F., Basu, S., Bertolacci, M., Bowman, K. W., et al.
927 (2023). Neutral tropical African CO₂ exchange estimated from aircraft and satellite

- 928 observations. *Global Biogeochemical Cycles*, 37, e2023GB007804.
929 <https://doi.org/10.1029/2023GB007804>
- 930 Goldberg L, Lagomasino D, Thomas N, Fatoyinbo T. (2020). Global declines in human-
931 driven mangrove loss. *Glob Change Biol*, 26: 5844–5855. <https://doi.org/10.1111/gcb.15275>
- 932 Haider, S., Swain, E., Beerens, J., Petkewich, M., McCloskey, B., and Henkel, H. (2020).
933 The Everglades Depth Estimation Network (EDEN) surface-water interpolation model,
934 version 3: U.S. Geological Survey Scientific Investigations Report 2020–5083, 31 p.,
935 <https://doi.org/10.3133/sir20205083>.
- 936 Hao, Q., Liu, F., Zhang, Y., Wang, O., & Xiao, L. (2020). Methylobacter accounts for strong
937 aerobic methane oxidation in the Yellow River Delta with characteristics of a methane sink
938 during the dry season. *Science of the Total Environment*, 704.
939 <https://doi.org/10.1016/j.scitotenv.2019.135383>
- 940 Hannun, R. A., Wolfe, G. M., Kawa, S. R., Hanisco, T. F., Newman, P. A., Alfieri, J. G.,
941 Barrick, J., Clark, K. L., Digangi, J. P., Diskin, G. S., King, J., Kustas, W. P., Mitra, B.,
942 Noormets, A., Nowak, J. B., Thornhill, K. L., & Vargas, R. (2020). Spatial heterogeneity in
943 CO₂, CH₄, and energy fluxes: insights from airborne eddy covariance measurements over
944 the Mid-Atlantic region. *Environmental Research Letters*, 15(3).
945 <https://doi.org/10.1088/1748-9326/ab7391>
- 946 Harrison, J. A., Deemer, B. R., Birchfield, M. K., & O'Malley, M. T. (2017). Reservoir
947 Water-Level Drawdowns Accelerate and Amplify Methane Emission. *Environmental*
948 *Science and Technology*, 51(3). <https://doi.org/10.1021/acs.est.6b03185>
- 949 Hawkes, C. v., Waring, B. G., Rocca, J. D., & Kivlin, S. N. (2017). Historical climate
950 controls soil respiration responses to current soil moisture. *Proceedings of the National*
951 *Academy of Sciences of the United States of America*, 114(24).
952 <https://doi.org/10.1073/pnas.1620811114>
- 953 Hayek, M. N., Wehr, R., Longo, M., Hutyra, L. R., Wiedemann, K., Munger, J. W., Bonal,
954 D., Saleska, S. R., Fitzjarrald, D. R., & Wofsy, S. C. (2018). A novel correction for biases in
955 forest eddy covariance carbon balance. *Agricultural and Forest Meteorology*, 250–251.
956 <https://doi.org/10.1016/j.agrformet.2017.12.186>
- 957 Hayes, D. J., Vargas, R., Alin, S., Conant, R. T., Hutyra, L. R., Jacobson, A. R., Kurz, W. A.,
958 Liu, S., McGuire, A. D., Poulter, B., & Woodall, C. W. (2018). The North American Carbon
959 Budget. Second State of the Carbon Cycle Report. Second State of the Carbon Cycle Report
960 (SOCCR2): A Sustained Assessment Report.
- 961 Högström, U. (1988). Non-dimensional wind and temperature profiles in the atmospheric
962 surface layer: A re-evaluation. *Boundary-Layer Meteorology*, 42(1–2).
963 <https://doi.org/10.1007/BF00119875>

- 964 Hondula, K. L., Jones, C. N., & Palmer, M. A. (2021). Effects of seasonal inundation on
965 methane fluxes from forested freshwater wetlands. *Environmental Research Letters*, 16(8).
966 <https://doi.org/10.1088/1748-9326/ac1193>
- 967 Hutjes, R. W. A., Vellinga, O. S., Gioli, B., & Miglietta, F. (2010). Dis-aggregation of
968 airborne flux measurements using footprint analysis. *Agricultural and Forest Meteorology*,
969 150(7–8). <https://doi.org/10.1016/j.agrformet.2010.03.004>
- 970 Iram, N., Kavehei, E., Maher, D. T., Bunn, S. E., Rezaei Rashti, M., Farahani, B. S., &
971 Adame, M. F. (2021). Soil greenhouse gas fluxes from tropical coastal wetlands and
972 alternative agricultural land uses. *Biogeosciences*, 18(18). [https://doi.org/10.5194/bg-18-](https://doi.org/10.5194/bg-18-5085-2021)
973 [5085-2021](https://doi.org/10.5194/bg-18-5085-2021)
- 974 Jha, C. S., Rodda, S. R., Thumaty, K. C., Raha, A. K., & Dadhwal, V. K. (2014). Eddy
975 covariance based methane flux in Sundarbans mangroves, India. *Journal of Earth System*
976 *Science*, 123(5). <https://doi.org/10.1007/s12040-014-0451-y>
- 977 Kljun, N., Calanca, P., Rotach, M. W., & Schmid, H. P. (2015). A simple two-dimensional
978 parameterisation for Flux Footprint Prediction (FFP). *Geoscientific Model Development*,
979 8(11). <https://doi.org/10.5194/gmd-8-3695-2015>
- 980 Kljun, N., Rotach, M. W., & Schmid, H. P. (2002). A three-dimensional backward
981 Lagrangian footprint model for a wide range of boundary-layer stratifications. *Boundary-*
982 *Layer Meteorology*, 103(2). <https://doi.org/10.1023/A:1014556300021>
- 983 Kristensen, E., Flindt, M. R., Ulomi, S., Borges, A. v., Abril, G., & Bouillon, S. (2008).
984 Emission of CO₂ and CH₄ to the atmosphere by sediments and open waters in two
985 Tanzanian mangrove forests. *Marine Ecology Progress Series*, 370.
986 <https://doi.org/10.3354/meps07642>
- 987 Kroeger, K. D., Crooks, S., Moseman-Valtierra, S., & Tang, J. (2017). Restoring tides to
988 reduce methane emissions in impounded wetlands: A new and potent Blue Carbon climate
989 change intervention. *Scientific Reports*, 7(1). <https://doi.org/10.1038/s41598-017-12138-4>
- 990 Lagomasino, D., Fatoyinbo, T., Castañeda-Moya, E., Cook, B. D., Montesano, P. M., Neigh,
991 C. S. R., Corp, L. A., Ott, L. E., Chavez, S., & Morton, D. C. (2021). Storm surge and
992 ponding explain mangrove dieback in southwest Florida following Hurricane Irma. *Nature*
993 *Communications*, 12(1). <https://doi.org/10.1038/s41467-021-24253-y>
- 994 Langford, B., Acton, W., Ammann, C., Valach, A., & Nemitz, E. (2015). Eddy-covariance
995 data with low signal-to-noise ratio: Time-lag determination, uncertainties and limit of
996 detection. *Atmospheric Measurement Techniques*, 8(10). [https://doi.org/10.5194/amt-8-4197-](https://doi.org/10.5194/amt-8-4197-2015)
997 [2015](https://doi.org/10.5194/amt-8-4197-2015)
- 998 Lee, S. C., Fan, C. J., Wu, Z. Y., & Juang, J. Y. (2015). Investigating effect of environmental
999 controls on dynamics of CO₂ budget in a subtropical estuarial marsh wetland ecosystem.
1000 *Environmental Research Letters*, 10(2). <https://doi.org/10.1088/1748-9326/10/2/025005>

- 1001 Lenschow, D. H., Mann, J., & Kristensen, L. (1994). How long is long enough when
1002 measuring fluxes and other turbulence statistics? *Journal of Atmospheric & Oceanic*
1003 *Technology*, 11(3). [https://doi.org/10.1175/1520-0426\(1994\)011<0661:HLILEW>2.0.CO;2](https://doi.org/10.1175/1520-0426(1994)011<0661:HLILEW>2.0.CO;2)
- 1004 Lin, C. W., Kao, Y. C., Chou, M. C., Wu, H. H., Ho, C. W., & Lin, H. J. (2020). Methane
1005 emissions from subtropical and tropical mangrove ecosystems in Taiwan. *Forests*, 11(4).
1006 <https://doi.org/10.3390/F11040470>
- 1007 Liu, J., & Lai, D. Y. F. (2019). Subtropical mangrove wetland is a stronger carbon dioxide
1008 sink in the dry than wet seasons. *Agricultural and Forest Meteorology*, 278.
1009 <https://doi.org/10.1016/j.agrformet.2019.107644>
- 1010 Ma, S., Worden, J. R., Bloom, A. A., Zhang, Y., Poulter, B., Cusworth, D. H., Yin, Y.,
1011 Pandey, S., Maasakkers, J. D., Lu, X., Shen, L., Sheng, J., Frankenberg, C., Miller, C. E., &
1012 Jacob, D. J. (2021). Satellite Constraints on the Latitudinal Distribution and Temperature
1013 Sensitivity of Wetland Methane Emissions. *AGU Advances*, 2(3).
1014 <https://doi.org/10.1029/2021av000408>
- 1015 Macreadie, P. I., Costa, M. D. P., Atwood, T. B., Friess, D. A., Kelleway, J. J., Kennedy, H.,
1016 Lovelock, C. E., Serrano, O., & Duarte, C. M. (2021). Blue carbon as a natural climate
1017 solution. In *Nature Reviews Earth and Environment* (Vol. 2, Issue 12).
1018 <https://doi.org/10.1038/s43017-021-00224-1>
- 1019 Malone, S. L., Keough, C., Staudhammer, C. L., Ryan, M. G., Parton, W. J., Olivas, P.,
1020 Oberbauer, S. F., Schedlbauer, J., & Starr, G. (2015). Ecosystem resistance in the face of
1021 climate change: A case study from the freshwater marshes of the Florida Everglades.
1022 *Ecosphere*, 6(4). <https://doi.org/10.1890/ES14-00404.1>
- 1023 Marín-Muñiz, J. L., Hernández, M. E., & Moreno-Casasola, P. (2015). Greenhouse gas
1024 emissions from coastal freshwater wetlands in Veracruz Mexico: Effect of plant community
1025 and seasonal dynamics. *Atmospheric Environment*, 107.
1026 <https://doi.org/10.1016/j.atmosenv.2015.02.036>
- 1027 McGowan, H. A., Lowry, A. L., & Gray, M. A. (2020). Identification of Optimum
1028 Temperatures for Photosynthetic Production in Subtropical Coastal Ecosystems: Implications
1029 for CO2 Sequestration in a Warming World. *Journal of Geophysical Research:*
1030 *Biogeosciences*, 125(8). <https://doi.org/10.1029/2020JG005678>
- 1031 McLeod, E., Chmura, G. L., Bouillon, S., Salm, R., Björk, M., Duarte, C. M., Lovelock, C.
1032 E., Schlesinger, W. H., & Silliman, B. R. (2011). A blueprint for blue carbon: Toward an
1033 improved understanding of the role of vegetated coastal habitats in sequestering CO2. In
1034 *Frontiers in Ecology and the Environment* (Vol. 9, Issue 10). <https://doi.org/10.1890/110004>
- 1035 Megonigal, J. P., & Guenther, A. B. (2008). Methane emissions from upland forest soils and
1036 vegetation. *Tree Physiology*, 28(4). <https://doi.org/10.1093/treephys/28.4.491>
- 1037 Melton, J. R., Wania, R., Hodson, E. L., Poulter, B., Ringeval, B., Spahni, R., Bohn, T., Avis,
1038 C. A., Beerling, D. J., Chen, G., Eliseev, A. v., Denisov, S. N., Hopcroft, P. O., Lettenmaier,

- 1039 D. P., Riley, W. J., Singarayer, J. S., Subin, Z. M., Tian, H., Zürcher, S., ... Kaplan, J. O.
1040 (2013). Present state of global wetland extent and wetland methane modelling: Conclusions
1041 from a model inter-comparison project (WETCHIMP). *Biogeosciences*, 10(2).
1042 <https://doi.org/10.5194/bg-10-753-2013>
- 1043 Moncrieff, J., Clement, R., Finnigan, J., & Meyers, T. (2006). Averaging, Detrending, and
1044 Filtering of Eddy Covariance Time Series. In *Handbook of Micrometeorology*.
1045 https://doi.org/10.1007/1-4020-2265-4_2
- 1046 Murray, N. J., Worthington, T. A., Bunting, P., Duce, S., Hagger, V., Lovelock, C. E., Lucas,
1047 R., Saunders, M. I., Sheaves, M., Spalding, M., Waltham, N. J., & Lyons, M. B. (2022).
1048 High-resolution mapping of losses and gains of Earth's tidal wetlands. *Science*, 376(6594).
1049 <https://doi.org/10.1126/science.abm9583>
- 1050 Murdiyarso, D., Purbopuspito, J., Kauffman, J. B., Warren, M. W., Sasmito, S. D., Donato,
1051 D. C., Manuri, S., Krisnawati, H., Taberima, S., & Kurnianto, S. (2015). The potential of
1052 Indonesian mangrove forests for global climate change mitigation. *Nature Climate Change*,
1053 5(12). <https://doi.org/10.1038/nclimate2734>
- 1054 Murguia-Flores, F., Jaramillo, V. J., & Gallego-Sala, A. (2023). Assessing Methane
1055 Emissions From Tropical Wetlands: Uncertainties From Natural Variability and Drivers at
1056 the Global Scale. In *Global Biogeochemical Cycles* (Vol. 37, Issue 9).
1057 <https://doi.org/10.1029/2022GB007601>
- 1058 Myneni, R., Knyazikhin, Y., Park, T. (2015). MCD15A2H MODIS/Terra+Aqua Leaf Area
1059 Index/FPAR 8-day L4 Global 500m SIN Grid V006 [Data set]. NASA EOSDIS Land
1060 Processes Distributed Active Archive Center. Accessed 2024-01-11 from
1061 <https://doi.org/10.5067/MODIS/MCD15A2H.006>
- 1062 Nahlik, A. M., & Mitsch, W. J. (2011). Methane emissions from tropical freshwater wetlands
1063 located in different climatic zones of Costa Rica. *Global Change Biology*, 17(3).
1064 <https://doi.org/10.1111/j.1365-2486.2010.02190.x>
- 1065 O'Neill, P. E., S. Chan, E. G. Njoku, T. Jackson, R. Bindlish, J. Chaubell, and A. Colliander.
1066 (2023). SMAP Enhanced L3 Radiometer Global and Polar Grid Daily 9 km EASE-Grid Soil
1067 Moisture, Version 6 [Data Set]. Boulder, Colorado USA. NASA National Snow and Ice Data
1068 Center Distributed Active Archive Center. <https://doi.org/10.5067/M20OXIZHY3RJ>. Date
1069 Accessed 11-11-2023.
- 1070 Orchard, V. A., & Cook, F. J. (1983). Relationship between soil respiration and soil
1071 moisture. *Soil Biology and Biochemistry*, 15(4). [https://doi.org/10.1016/0038-0717\(83\)90010-X](https://doi.org/10.1016/0038-0717(83)90010-X)
- 1073 Pandey, S., Houweling, S., Lorente, A., Borsdorff, T., Tsvilidou, M., Anthony Bloom, A.,
1074 Poulter, B., Zhang, Z., & Aben, I. (2021). Using satellite data to identify the methane
1075 emission controls of South Sudan's wetlands. *Biogeosciences*, 18(2).
1076 <https://doi.org/10.5194/bg-18-557-2021>

- 1077 Poulter, B., Adams-Metayer, F. M., Amaral, C., Barenblitt, A., Campbell, A., Charles, S. P.,
1078 Roman-Cuesta, R. M., D'Ascanio, R., Delaria, E. R., Doughty, C., Fatoyinbo, T.,
1079 Gewirtzman, J., Hanisco, T. F., Hull, M., Kawa, S. R., Hannun, R., Lagomasino, D., Lait, L.,
1080 Malone, S. L., ... Zhang, Z. (2023). Multi-scale observations of mangrove blue carbon
1081 ecosystem fluxes: The NASA Carbon Monitoring System BlueFlux field campaign.
1082 *Environmental Research Letters*, 18(7). <https://doi.org/10.1088/1748-9326/acdae6>
- 1083 Rivera-Monroy, V. H., Danielson, T. M., Castañeda-Moya, E., Marx, B. D., Travieso, R.,
1084 Zhao, X., Gaiser, E. E., & Farfan, L. M. (2019). Long-term demography and stem
1085 productivity of Everglades mangrove forests (Florida, USA): Resistance to hurricane
1086 disturbance. *Forest Ecology and Management*, 440.
1087 <https://doi.org/10.1016/j.foreco.2019.02.036>
- 1088 Rosentreter, J. A., Maher, D. T., Erler, D. v., Murray, R., & Eyre, B. D. (2018a). Factors
1089 controlling seasonal CO₂ and CH₄ emissions in three tropical mangrove-dominated estuaries
1090 in Australia. *Estuarine, Coastal and Shelf Science*, 215.
1091 <https://doi.org/10.1016/j.ecss.2018.10.003>
- 1092 Rosentreter, J. A., Maher, D. T., Erler, D. v., Murray, R., & Eyre, B. D. (2018b). Seasonal
1093 and temporal CO₂ dynamics in three tropical mangrove creeks – A revision of global
1094 mangrove CO₂ emissions. *Geochimica et Cosmochimica Acta*, 222.
1095 <https://doi.org/10.1016/j.gca.2017.11.026>
- 1096 Rosentreter, J. A., Maher, D. T., Erler, D. v., Murray, R. H., & Eyre, B. D. (2018c). Methane
1097 emissions partially offset “blue carbon” burial in mangroves. *Science Advances*, 4(6).
1098 <https://doi.org/10.1126/sciadv.aao4985>
- 1099 Rosentreter, J. A., Borges, A. v., Deemer, B. R., Holgerson, M. A., Liu, S., Song, C., Melack,
1100 J., Raymond, P. A., Duarte, C. M., Allen, G. H., Olefeldt, D., Poulter, B., Battin, T. I., &
1101 Eyre, B. D. (2021). Half of global methane emissions come from highly variable aquatic
1102 ecosystem sources. *Nature Geoscience*, 14(4). <https://doi.org/10.1038/s41561-021-00715-2>
- 1103 Ross, M. S., Ruiz, P. L., Sah, J. P., & Hanan, E. J. (2009). Chilling damage in a changing
1104 climate in coastal landscapes of the subtropical zone: A case study from south Florida.
1105 *Global Change Biology*, 15(7). <https://doi.org/10.1111/j.1365-2486.2009.01900.x>
- 1106 Ruiz, P. L., A. Lee, C. Thompson, I. Castillo, M. Guichardot, C. P. Perry, A. Arteaga Garcia,
1107 M. Foguer, M. C. Prats, E. Garcia, S. Lamosa, R. B. Shamblin, and K. R. T. Whelan. (2019).
1108 The Everglades National Park and Big Cypress National Preserve vegetation mapping
1109 project: Interim report—Eastern Big Cypress (Regions 5 & 6), Big Cypress National
1110 Preserve. Natural Resource Report NPS/SFCN/NRR—2019/2035. National Park Service,
1111 Fort Collins, Colorado.
- 1112 Ruiz, P. L., T. N. Schall, R. B. Shamblin, and K. R. T. Whelan. (2021). The vegetation of
1113 Everglades National Park: Final report. Natural Resource Report NPS/SFCN/NRR—
1114 2021/2256. National Park Service, Fort Collins, Colorado. [https://doi.org/10.36967/nrr-
1115 2286460](https://doi.org/10.36967/nrr-2286460).

- 1116 Sanderman, J., Hengl, T., Fiske, G., Solvik, K., Adame, M. F., Benson, L., Bukoski, J. J.,
1117 Carnell, P., Cifuentes-Jara, M., Donato, D., Duncan, C., Eid, E. M., Ermgassen, P. Z., Lewis,
1118 C. J. E., Macreadie, P. I., Glass, L., Gress, S., Jardine, S. L., Jones, T. G., ... Landis, E.
1119 (2018). A global map of mangrove forest soil carbon at 30 m spatial resolution.
1120 *Environmental Research Letters*, 13(5). <https://doi.org/10.1088/1748-9326/aabe1c>
- 1121 Saunois, M., R. Stavert, A., Poulter, B., Bousquet, P., G. Canadell, J., B. Jackson, R., A.
1122 Raymond, P., J. Dlugokencky, E., Houweling, S., K. Patra, P., Ciais, P., K. Arora, V.,
1123 Bastviken, D., Bergamaschi, P., R. Blake, D., Brailsford, G., Bruhwiler, L., M. Carlson, K.,
1124 Carrol, M., ... Zhuang, Q. (2020). The global methane budget 2000-2017. *Earth System*
1125 *Science Data*, 12(3). <https://doi.org/10.5194/essd-12-1561-2020>
- 1126 Schedlbauer, J. L., Munyon, J. W., Oberbauer, S. F., Gaiser, E. E., & Starr, G. (2012).
1127 Controls on ecosystem carbon dioxide exchange in short- and long-hydroperiod Florida
1128 everglades freshwater marshes. *Wetlands*, 32(5). <https://doi.org/10.1007/s13157-012-0311-y>
- 1129 Schiferl, L. D., Watts, J. D., Larson, E. J. L., Arndt, K. A., Biraud, S. C., Euskirchen, E. S.,
1130 Goodrich, J. P., Henderson, J. M., Kalhori, A., Mckain, K., Mountain, M. E., Munger, J. W.,
1131 Oechel, W. C., Sweeney, C., Yi, Y., Zona, D., & Commane, R. (2022). Using atmospheric
1132 observations to quantify annual biogenic carbon dioxide fluxes on the Alaska North Slope.
1133 *Biogeosciences*, 19(24). <https://doi.org/10.5194/bg-19-5953-2022>
- 1134 Sellers, P. J., Hall, F. G., Kelly, R. D., Black, A., Baldocchi, D., Berry, J., Ryan, M., Ranson,
1135 K. J., Crill, P. M., Lettenmaier, D. P., Margolis, H., Cihlar, J., Newcomer, J., Fitzjarrald, D.,
1136 Jarvis, P. G., Gower, S. T., Halliwell, D., Williams, D., Goodison, B., ... Guertin, F. E.
1137 (1997). BOREAS in 1997: Experiment overview, scientific results, and future directions.
1138 *Journal of Geophysical Research Atmospheres*, 102(24). <https://doi.org/10.1029/97jd03300>
- 1139 Shaw, J. T., Allen, G., Barker, P., Pitt, J. R., Pasternak, D., Bauguitte, S. J.-B., et al. (2022).
1140 Large methane emission fluxes observed from tropical wetlands in Zambia. *Global*
1141 *Biogeochemical Cycles*, 36, e2021GB007261. <https://doi.org/10.1029/2021GB007261>
- 1142 Shoemaker, W. B., Anderson, F., Barr, J. G., Graham, S. L., & Botkin, D. B. (2015). Carbon
1143 exchange between the atmosphere and subtropical forested cypress and pine wetlands.
1144 *Biogeosciences*, 12(8). <https://doi.org/10.5194/bg-12-2285-2015>
- 1145 Simard, M., Fatoyinbo, L., Smetanka, C., Rivera-Monroy, V. H., Castañeda-Moya, E.,
1146 Thomas, N., & van der Stocken, T. (2019). Mangrove canopy height globally related to
1147 precipitation, temperature and cyclone frequency. *Nature Geoscience*, 12(1).
1148 <https://doi.org/10.1038/s41561-018-0279-1>
- 1149 Smith, T. J., Anderson, G. H., Balentine, K., Tiling, G., Ward, G. A., & Whelan, K. R. T.
1150 (2009). Cumulative impacts of hurricanes on Florida mangrove ecosystems: Sediment
1151 deposition, storm surges and vegetation. *Wetlands*, 29(1). <https://doi.org/10.1672/08-40.1>
- 1152 Souza, R. B., Copertino, M. S., Fisch, G., Santini, M. F., Pinaya, W. H. D., Furlan, F. M.,
1153 Alves, R. de C. M., Möller, O. O., & Pezzi, L. P. (2022). Salt marsh-atmosphere CO₂

- 1154 exchanges in Patos Lagoon Estuary, Southern Brazil. *Frontiers in Marine Science*, 9.
1155 <https://doi.org/10.3389/fmars.2022.892857>
- 1156 Taillie, P. J., Roman-Cuesta, R., Lagomasino, D., Cifuentes-Jara, M., Fatoyinbo, T., Ott, L.
1157 E., & Poulter, B. (2020). Widespread mangrove damage resulting from the 2017 Atlantic
1158 mega hurricane season. *Environmental Research Letters*, 15(6). [https://doi.org/10.1088/1748-](https://doi.org/10.1088/1748-9326/ab82cf)
1159 [9326/ab82cf](https://doi.org/10.1088/1748-9326/ab82cf)
- 1160 Torrence, C., & Compo, G. P. (1998). A Practical Guide to Wavelet Analysis. *Bulletin of the*
1161 *American Meteorological Society*, 79(1). [https://doi.org/10.1175/1520-](https://doi.org/10.1175/1520-0477(1998)079<0061:APGTWA>2.0.CO;2)
1162 [0477\(1998\)079<0061:APGTWA>2.0.CO;2](https://doi.org/10.1175/1520-0477(1998)079<0061:APGTWA>2.0.CO;2)
- 1163 Troxler, T. G., Gaiser, E., Barr, J., Fuentes, J. D., Jaffé, R., Childers, D. L., Colado-Vides, L.,
1164 Rivera-Monroy, V. H., Castañeda-Moya, E., Anderson, W., Chambers, R., Chen, M.,
1165 Coronado-Molina, C., Davis, S. E., Engel, V., Fitz, C., Fourqurean, J., Frankovich, T.,
1166 Kominoski, J., Madden C., Malone S., Oberbauer S., Olivas P., Richards J., Saunders C.,
1167 Schedlbauer J., Scinto L., Sklar F., Smith T., Smoak J., Starr G., Twilley R., Whelan, K.
1168 (2013). Integrated carbon budget models for the everglades terrestrial-coastal-oceanic
1169 gradient: Current status and needs for inter-site comparisons. *Oceanography*, 26(3).
1170 <https://doi.org/10.5670/oceanog.2013.51>
- 1171 Troxler, T. G., Barr, J. G., Fuentes, J. D., Engel, V., Anderson, G., Sanchez, C., Lagomasino,
1172 D., Price, R., & Davis, S. E. (2015). Component-specific dynamics of riverine mangrove
1173 CO₂ efflux in the Florida coastal Everglades. *Agricultural and Forest Meteorology*, 213.
1174 <https://doi.org/10.1016/j.agrformet.2014.12.012>
- 1175 Wang, J. S., Randolph Kawa, S., James Collatz, G., Sasakawa, M., Gatti, L. v., Machida, T.,
1176 Liu, Y., & Manyin, M. E. (2018). A global synthesis inversion analysis of recent variability
1177 in CO₂ fluxes using GOSAT and in situ observations. *Atmospheric Chemistry and Physics*,
1178 18(15). <https://doi.org/10.5194/acp-18-11097-2018>
- 1179 Whelan, K. R. T., M. Prats, and A. J. Atkinson. (2020). Western Big Cypress National
1180 Preserve vegetation map. Natural Resource Report NPS/SFCN/NRR—2020/2170. National
1181 Park Service, Fort Collins, Colorado. <https://doi.org/10.36967/nrr-2278240>.
- 1182 Wolfe, G. M., Hanisco, T. F., Arkinson, H. L., Bui, T. P., Crouse, J. D., Dean-Day, J.,
1183 Goldstein, A., Guenther, A., Hall, S. R., Huey, G., et al. (2015), Quantifying sources and
1184 sinks of reactive gases in the lower atmosphere using airborne flux observations, *Geophys.*
1185 *Res. Lett.*, 42, 8231–8240, doi:10.1002/2015GL065839.
- 1186 Wolfe, G. M., Kawa, S. R., Hanisco, T. F., Hannun, R. A., Newman, P. A., Swanson, A.,
1187 Bailey, S., Barrick, J., Thornhill, K. L., Diskin, G., DiGangi, J., Nowak, J. B., Sorenson, C.,
1188 Bland, G., Yungel, J. K., and Swenson, C. A. (2018). The NASA Carbon Airborne Flux
1189 Experiment (CARAFE): instrumentation and methodology, *Atmos. Meas. Tech.*, 11, 1757–
1190 [1776, https://doi.org/10.5194/amt-11-1757-2018](https://doi.org/10.5194/amt-11-1757-2018)
- 1191 Xiong, L., Lagomasino, D., Charles, S. P., Castañeda-Moya, E., Cook, B. D., Redwine, J., &
1192 Fatoyinbo, L. (2022). Quantifying mangrove canopy regrowth and recovery after Hurricane

- 1193 Irma with large-scale repeat airborne lidar in the Florida Everglades. *International Journal of*
1194 *Applied Earth Observation and Geoinformation*, 114.
1195 <https://doi.org/10.1016/j.jag.2022.103031>
- 1196 Zhang, Z., Poulter, B., Feldman, A. F., Ying, Q., Ciais, P., Peng, S., & Li, X. (2023). Recent
1197 intensification of wetland methane feedback. *Nature Climate Change*, 13(5).
1198 <https://doi.org/10.1038/s41558-023-01629-0>
- 1199 Zhao, J., S. L. Malone, C. L. Staudhammer, G. Starr, H. Hartmann, S. F. Oberbauer (2021).
1200 Wetland plants respond nonlinearly to inundation over a sustained period. *American Journal*
1201 *of Botany*.108, 1917-1931.
- 1202 Zhu, X., Qin, Z., & Song, L. (2021). How Land-Sea Interaction of Tidal and Sea Breeze
1203 Activity Affect Mangrove Net Ecosystem Exchange? *Journal of Geophysical Research:*
1204 *Atmospheres*, 126(8). <https://doi.org/10.1029/2020JD034047>
- 1205 Zulueta, R. C., Oechel, W. C., Verfaillie, J. G., Hastings, S. J., Gioli, B., Lawrence, W. T., &
1206 Paw U, K. T. (2013). Aircraft regional-scale flux measurements over complex landscapes of
1207 Mangroves, desert, and marine ecosystems of Magdalena Bay, Mexico. *Journal of*
1208 *Atmospheric and Oceanic Technology*, 30(7). <https://doi.org/10.1175/JTECH-D-12-00022.1>
1209